CONF-9505200--

Proceedings of the THIRTEENTH SYMPOSIUM ON ENERGY ENGINEERING SCIENCES

Fluid/Thermal Processes; Systems Analysis and Control

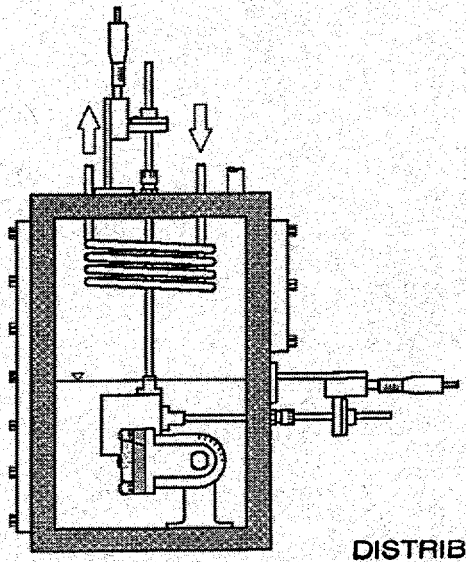

May 15-17, 1995
at
Argonne
National Laboratory
Argonne, Illinois

CONF-9505200

Proceedings of the

THIRTEENTH SYMPOSIUM ON ENERGY ENGINEERING SCIENCES
Fluid/Thermal Processes; Systems Analysis and Control

May 15-17, 1995

at

ARGONNE NATIONAL LABORATORY

Argonne, Illinois

Cosponsored by

Office of Basic Energy Sciences
U.S. DEPARTMENT OF ENERGY

and

Energy Technology Division
ARGONNE NATIONAL LABORATORY

Coordinated by

Argonne National Laboratory
9700 South Cass Avenue
Argonne, Illinois 60439

THIRTEENTH SYMPOSIUM ON ENERGY ENGINEERING SCIENCES
Fluid/Thermal Processes; Systems Analysis and Control

FOREWORD

This Proceedings Volume includes the technical papers that were presented during the Thirteenth Symposium on Energy Engineering Sciences on May 15-17, 1995, at Argonne National Laboratory, Argonne, Illinois. The Symposium was organized into nine technical sessions, which included 33 individual presentations followed by discussion and interaction with the audience. A copy of the schedule and a list of participants is appended to this volume.

This was the thirteenth annual Symposium sponsored by the Engineering Research Program of the Office of Basic Energy Sciences of the U.S. Department of Energy. The technical areas encompassed in this year's Symposium were fluid and thermal processes, and systems analysis and control. The dominant theme was fluid mechanics, which constituted five of the sessions and included 19 individual presentations. Each paper dealt with the research effort being sponsored by the Engineering Research Program.

The DOE Office of Basic Energy Sciences, of which Engineering Research is a component program, is responsible for the long-term mission-oriented research in the Department. It has the prime responsibility for establishing the basic scientific foundation upon which the Nation's future energy options will have to be identified, developed, and built. It is committed to the generation of new knowledge necessary for the solution of present and future problems of energy exploration, production, conversion, and utilization, consistent with respect for the environment.

Consistent with the DOE/BES mission, the Engineering Research Program is charged with the identification, initiation, and management of fundamental research on broad, generic topics addressing energy-related engineering problems. Its stated goals are: 1) to improve and extend the body of knowledge underlying current engineering practice so as to create new options for enhancing energy savings and production, for prolonging useful life of energy-related structures and equipment, and for developing advanced manufacturing technologies and materials processing with emphasis on reducing costs with improved industrial production and performance quality; and 2) to expand the store of fundamental concepts for solving anticipated and unforeseen engineering problems in the energy technologies.

In achieving these goals, the Engineering Research Program supports approximately 130 research projects covering a broad spectrum of topics cutting across traditional engineering disciplines with a focus on three areas: 1) mechanical sciences, 2) control systems and instrumentation, and 3) engineering data and analysis. The Thirteenth Symposium involved approximately one-fourth of the research projects currently sponsored by the DOE/BES Engineering Research Program.

The Thirteenth Symposium was held under the joint sponsorship of the DOE Office of Basic Energy Sciences and Argonne National Laboratory. Local arrangements were handled by Ms. Jacquie Habenicht of ANL Conference Services. Ms. Nina Daly of the ANL Office of Technical Communication Services was responsible for assembling these proceedings and attending to their publication.

I am grateful to all who contributed to the success of the program, particularly to the participants for their uniformly excellent presentations, their active involvement in discussions, and their

infectious enthusiasm. The resulting interactions made this Symposium a most stimulating and enjoyable experience.

James R. Welty, ER-15
Division of Engineering and Geosciences
Office of Basic Energy Sciences

THIRTEENTH SYMPOSIUM ON ENERGY ENGINEERING SCIENCES

May 15-17, 1995

Argonne National Laboratory

Argonne, IL

FINAL PROGRAM

Monday, May 15

8:00 a.m. Registration

9:00 a.m. Welcome

9:05 a.m. General Remarks
Oscar P. Manley, U.S. Department of Energy

9:10 a.m. Introductory Comments
James R. Welty, U.S. Department of Energy

TECHNICAL SESSION 1 - Fluid Mechanics I: Fundamental Properties

Chair: E. Fukushima, Lovelace Foundation

9:15 a.m. Viscosity of Colloidal Suspensions
E.G.D. Cohen, The Rockefeller Univ., New York and I.M. de Schepper, Delft University of Technology, The Netherlands

9:40 a.m. Gelation Under Shear
B.D. Butler, H.J.M. Hanley, G.C. Straty, and C.D. Muzny, NIST, Boulder, CO

10:05 a.m. Transport Properties of Porous Media from the Microstructure
S. Torquato, Princeton Univ., Princeton, NJ

10:30 a.m. BREAK

TECHNICAL SESSION 2 - Fluid Mechanics II: Two-Phase Flow

Chair: S. Torquato, Princeton University

10:45 a.m. NMR Studies of Multiphase Flows. II
S.A. Altobelli, A. Caprihan, E. Fukushima, I.J. Lowe, and L.Z. Wang, The Lovelace Inst., Albuquerque, NM

11:10 a.m.	Initiation of Slug Flow T.J. Hanratty and B.D. Woods, Univ. of Illinois, Urbana, IL
11:35 a.m.	The Drift Force on an Object in an Inviscid Weakly-Varying Rotational Flow G.B. Wallis, Dartmouth College, Hanover, NH
12:00 noon	LUNCH

TECHNICAL SESSION 3 - Thermal Processes

Chair: G. Pomraning, U.C.L.A.

1:00 p.m.	Active Control of Convection H.H. Bau, Univ. of Pennsylvania, Philadelphia, PA
1:25 p.m.	Effect of Steady and Time-Harmonic Magnetic Fields on Macrosegregation in Alloy Solidification F.P. Incropera and P.J. Prescott, Purdue U., W. Lafayette, IN
1:50 p.m.	Theoretical Modeling of CHF for Near-Saturated Pool Boiling and Flow Boiling from Short Heaters Using the Interfacial Lift-Off Criterion I. Mudawar, J.E. Galloway, C.O. Gersey, S.J. Reed, and D.D. Hall, Purdue Univ., W. Lafayette, IN
2:15 p.m.	Short-Pulse Laser Interactions with Disordered Materials and Liquids L.M. Phinney, C.H. Goldman, J.P. Longtin, and C.-L. Tien, Univ. of California, Berkeley, CA
2:50 p.m.	BREAK

TECHNICAL SESSION 4 - Fluid Mechanics III

Chair: I. Mudawar, Purdue University

3:05 p.m.	Studies on the Formulation of Thermodynamics and Stochastic Theory for Systems Far From Equilibrium J. Ross, Stanford Univ., Stanford, CA
3:30 p.m.	Linear Kinetic Theory and Particle Transport in Stochastic Mixtures G.C. Pomraning, UCLA, Los Angeles, CA
3:55 p.m.	Dynamics of Miscible Displacements in Round Tubes E. Meiburg, T. Maxworthy, P. Petijeans, and C.-Y. Chen, Univ. of Southern California, Los Angeles, CA
4:20 p.m.	Superconducting Coherence in a Vortex Line Liquid T. Chen and S. Teitel, Univ. of Rochester, Rochester, NY

5:30 p.m. RECEPTION

6:00 p.m. SYMPOSIUM DINNER

Tuesday, May 16

TECHNICAL SESSION 5 - Process Analysis and Control

Chair: J.B. McLaughlin, Clarkson University

8:25 a.m. Systematic Process Synthesis and Design Methods for Cost Effective Waste Minimization
L.T. Biegler, I.E. Grossmann, and A.W. Westerberg, Carnegie Mellon Univ., Pittsburgh, PA

8:50 a.m. Integrated Approaches to the Application of Advanced Modeling Technology in Process Development and Optimization
R.J. Allgor, W.F. Feehery, J.E. Tolsma, L.B. Evans, and P.I. Barton, MIT, Cambridge, MA

9:15 a.m. Intelligent Control of Mixed-Culture Bioprocesses
D.L. Stoner, E.D. Larsen, K.S. Miller, G.F. Andrews, and J.A. Johnson, INEL, Idaho Falls, ID

9:40 a.m. Control of Complex Dynamics and Chaos in Distributed Parameter Systems
S. Chakravarti, M. Marek, and W.H. Ray, Univ. of Wisconsin, Madison, WI

10:05 a.m. BREAK

TECHNICAL SESSION 6 - Fluid Mechanics IV: Turbulence

Chair: J. Ottino, Northwestern University

10:20 a.m. Turbulence Generation by Waves
D. Kaftori, X.S. Nan, and S. Banerjee, Univ. of California, Santa Barbara, CA

10:45 a.m. Numerical Simulation of High Reynolds Number Bubble Motion
J.B. McLaughlin, Clarkson Univ., Potsdam, NY

11:10 a.m. Structure and Modeling of Turbulence
E.A. Novikov, Univ. of Calif., San Diego, CA

11:35 a.m. Contaminant Dispersal in Bounded Turbulent Shear Flow
J.M. Wallace, P.S. Bernard, K.-F. Chiang, and L. Ong, Univ. of Maryland, College Park, MD

12:00 noon — Anomalous Scaling of a Scalar Field Advected by Turbulence
R.H. Kraichnan, R.H. Kraichnan, Inc., Santa Fe, NM

12:25 — LUNCH

TECHNICAL SESSION 7 - Fluid Mechanics V: Chaos

Chair: J. Wallace, University of Maryland

1:25 p.m. — Convection in a Nematic Liquid Crystal With Homeotropic Alignment and Heated From Below
G. Ahlers, Univ. of California, Santa Barbara, CA

1:50 p.m. — Modeling of Mixing Processes: Fluids, Particulates, and Powders
J.M. Ottino and S. Hansen, Northwestern Univ., Evanston, IL

2:15 p.m. — Spatiotemporal Patterns in a Reaction-Diffusion System and in a Vibrated Granular Bed
H.L. Swinney, K.J. Lee, W.D. McCormick, F. Melo, and P. Umbanhowar, Univ. of Texas, Austin, TX

2:40 p.m. — BREAK

TECHNICAL SESSION 8 - Materials Issues

Chair: J. Heberlein, University of Minnesota

2:55 p.m. — Deformation and Crack Growth Response Under Cyclic Creep Conditions
F.W. Brust, Jr., Battelle Mem. Inst., Columbus, OH

3:20 p.m. — Advanced Laser Diagnostics for Diamond Deposition Research
C.H. Kruger, T.G. Owano, and E.H. Wahl, Stanford Univ., Stanford, CA

3:45 p.m. — Physical Models of Polarization Mode Dispersion
C.R. Menyuk and P.K.A. Wai, Univ. of Maryland, Baltimore, MD

4:10 p.m. — Conditions for Synchronization in Josephson-Junction Arrays
A.A. Chernikov and G. Schmidt, Stevens Inst. of Tech., Hoboken, NJ

Wednesday, May 17

TECHNICAL SESSION 9 - Plasma Processes

Chair: J. Welty, U.S. Department of Energy

8:25 a.m. — Modeling Electronegative Plasma Discharge
A.J. Lichtenberg and M.A. Lieberman, Univ. of California, Berkeley, CA

8:50 a.m.	Plasma Characterization Studies for Materials Processing E. Pfender and J. Heberlein, Univ. of Minnesota, Minneapolis, MN
9:15 a.m.	Hydrodynamic Theory of Diffusion in Two-Temperature Multicomponent Plasmas J.D. Ramshaw and C.H. Chang, INEL, Idaho Falls, ID
9:40 a.m.	Closing Remarks Oscar P. Manley, U.S. Department of Energy
10:00 a.m.	Meeting Adjourns

Table of Contents

VISCOSITY OF COLLOIDAL SUSPENSIONS

E. G. D. Cohen*
and
I. M. de Schepper**

*The Rockefeller University
New York, NY 10021, U.S.A.
**Delft University of Technology
2629 JB Delft, The Netherlands

ABSTRACT

Simple expressions are given for the effective Newtonian viscosity as a function of concentration as well as for the effective visco-elastic response as a function of concentration and imposed frequency, of monodisperse neutral colloidal suspensions over the entire fluid range. The basic physical mechanisms underlying these formulae are discussed. The agreement with existing experiments is very good.

INTRODUCTION

We discuss here suspensions consisting of monodisperse spherical neutral colloidal particles with a diameter σ. The problem we address is: in the absence of hydrodynamic interactions, what is the effective viscosity of such a suspension, i.e., its viscosity as different from η_s, the viscosity of the pure solvent? We are interested in this as a function of the volume fraction $\phi = \pi n \sigma^3/6$ of the colloidal particles, viz. $\eta^{\text{eff}}(\phi)$, its effective Newtonian viscosity or $\eta^{\text{eff}}(\phi;\omega)$ its effective visco-elastic viscosity, when an imposed oscillatory shear rate $\gamma(t) = \gamma e^{i\omega t}$ of frequency ω is present. Here n is the number density of the colloidal particles and γ the amplitude of the imposed shear rate.

This is a very difficult problem, since it concerns a strongly interacting many particle system, especially at large volume fractions. It is part of a large class of "effective" behavior problems, which can usually only be treated in a systematic way at small ϕ by cluster expansions. Here we outline an approximate, yet satisfactory solution of this problem, derived from first principles, which leads to explicit formulae for $\eta^{\text{eff}}(\phi) \equiv \eta^{\text{eff}}(\phi;\omega = 0)$ and $\eta^{\text{eff}}(\phi;\omega)$, which agree with experiment and therefore appear to contain the right physics. In the next section we briefly outline the steps that lead from the fundamental Smoluchowski equation to the basic equation we use to compute $\eta^{\text{eff}}(\phi;\omega)$. In the following section we present the solution of this equation, the explicit formulae for $\eta^{\text{eff}}(\phi)$ and $\eta^{\text{eff}}(\phi;\omega)$ and a comparison of them with experiment. In the last section, we discuss our results.

THEORY

Basic Equation.

Starting from the N particle Smoluchowski equation in the absence of hydrodynamic interactions and integrating this equation over the positions of all particles but two, one obtains an

equation for the nonequilibrium pair distribution function $P_2(\mathbf{R};\mathbf{r};\phi;\omega;t)$ of the suspension, involving the three-particle distribution function P_3. Neglecting P_3 and the dependence of P_2 on the center of mass $\mathbf{R} = (\mathbf{r}_1 + \mathbf{r}_2)/2$ of the two particles at positions $\mathbf{r}_i (i = 1, 2)$, respectively, and making a Fourier transform of P_2 with respect to the relative coordinate $\mathbf{r} = \mathbf{r}_1 - \mathbf{r}_2$, one arrives at an equation of the form[1,2]

$$[\frac{\partial}{\partial t} + \frac{2}{\tau(k;\phi)} - \gamma e^{i\omega t} k_y \frac{\partial}{\partial k_x}]\delta S(\mathbf{k};\phi;\omega;t) = \gamma e^{i\omega t} k_y \frac{\partial}{\partial k_x} S_{eq}(k;\phi) \qquad (1)$$

Here $\delta S(\mathbf{k};\phi;\omega;t) = S(\mathbf{k};\phi;\omega;t) - S_{eq}(k;\phi)$ is the deviation of the nonequilibrium structure factor $S(\mathbf{k};\phi;\omega;t)$, the Fourier transform of $P_2(\mathbf{r};\phi;\omega;t)$, from that in equilibrium $S_{eq}(k;\phi)$, the Fourier transform of the equilibrium radial distribution function $g(r;\phi)$, where $r = |\mathbf{r}|$ and $k = |\mathbf{k}|$. $S_{eq}(k;\phi)$ is known for hard spheres[3] and exhibits for $0.3 < \phi < 0.55$ a very sharp maximum at $k \approx k^*$, where $k^*\sigma \approx 2\pi$, i.e., for periodic particle configurations with a wave length $\lambda^* = 2\pi/k^* \approx \sigma$ (cf.fig.1). This sharp maximum at these large ϕ reflects a highly ordered state of the colloidal particles in the suspension on this length scale (cf.fig.2), where each particle finds itself in a cage formed by its nearest neighbors, out of which it can only escape, i.e., diffuse, with difficulty[2,4]. At

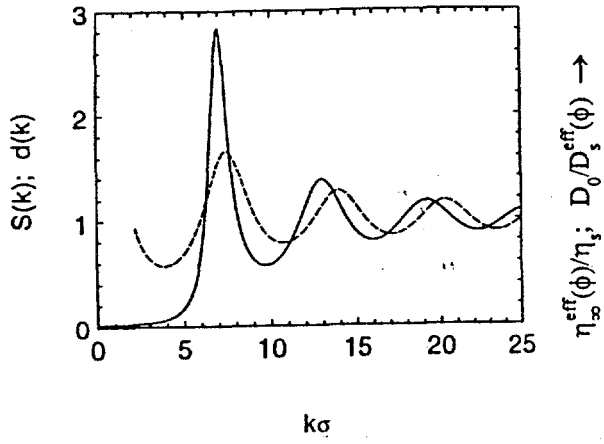

Figure 1 (left). Hard sphere S(k) for $\phi = 0.49$ (solid line, cf.Ref.3) and d(k) (dashed line, cf.below Eq.2), as functions of $k\sigma$.

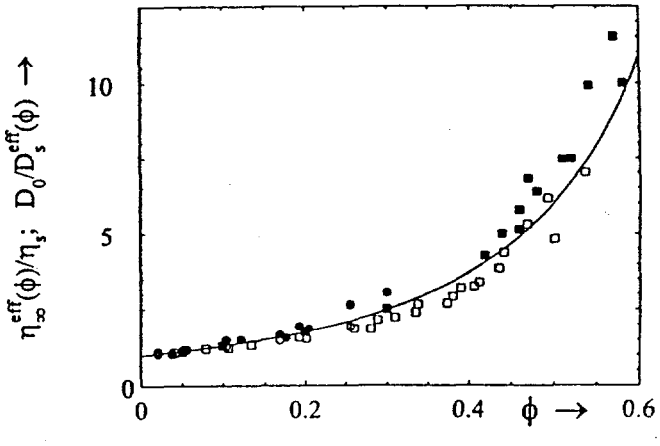

Figure 3 (right). Reduced high frequency viscosity $\eta_\infty^{eff}(\phi)/\eta_s$ (closed symbols) and inverse self diffusion $D_0/D_s^{eff}(\phi)$ (open symbols) as a function of ϕ. Open and closed circles from Ref.9(a), open squares from Ref.9(b) and closed squares from Ref.10. The solid line is $\chi(\phi)$ (cf.Eq.(4)); deviations due to hydrodynamic effects for intermediate ϕ (open squares) are visible.

small ϕ, $S_{eq}(k;\phi)$ displays no such maximum and the colloidal particle diffusion approaches that of free colloidal particles characterized by D_0, the Stokes-Einstein diffusion coefficient. The inverse relaxation time $1/\tau(k;\phi)$ in eq.(1) approaches D_0k^2 for small ϕ and is determined for large ϕ, by a cage-diffusion coefficient $D_c(k)$, derived from the analogous cage diffusion process in (pure) dense hard sphere fluids, by replacing the low density hard sphere gas Boltzmann diffusion coefficient D_B by the Stokes-Einstein diffusion coefficient D_0, relevant for dilute colloidal suspensions[1,2,4-7]:

$$1/\tau(k;\phi) = D_c(k)k^2 = \frac{D_0k^2}{\chi(\phi)S_{eq}(k;\phi)}d(k) \;\; (0.3 < \phi < 0.55) \qquad (2)$$

Here the equilibrium radial distribution function $g(r;\phi)$ at contact $r = \sigma : g(\sigma;\phi) \equiv \chi(\phi)$ is given very well by the Carnahan-Starling approximation $\chi(\phi) \approx (1 - \phi/2)(1 - \phi)^{-3} = 1 + \frac{5}{2}\phi + O(\phi^2)$, where the $O(\phi)$) term is exact (cf.fig.3) and $d(k) = 1/[1 - j_0(k\sigma) + 2j_2(k\sigma)]$, with $j_\ell(k\sigma)$ the ℓ-th spherical Bessel function (cf.fig.1). $1/\tau(k;\phi)$ is sketched and compared with the results of light scattering experiments in fig.4 for a typical large ϕ[6,7].

Solution and effective viscosity.

Solving the eq.(1) for $\delta S(\mathbf{k};\phi;\omega;t)$, integrating the solution over k and t and setting $\gamma = 0$, one obtains for the visco-elastic behavior of the colloidal suspension:

$$\eta^{\text{eff}}(\phi;\omega) = \eta^{\text{eff}}_{\infty}(\phi) + \frac{k_B T}{60\pi^2}\int_0^{\infty} dk\, k^4 [\frac{S'_{eq}(k;\phi)}{S_{eq}(k;\phi)}]^2 \frac{1}{2D_c(k)k^2 - i\omega} \quad (3)$$

Here $\eta^{\text{eff}}_{\infty}(\phi)$ is the infinite frequency, i.e., very short time, approximation to $\eta^{\text{eff}}(\phi;\omega)$ given by:

$$\eta^{\text{eff}}_{\infty}(\phi) = \eta_s \chi(\phi) \quad (4)$$

while $S'_{eq}(k;\phi) = dS_{eq}(k;\phi)/dk$. The second term on the right hand side of (3) is the contribution due to cage-diffusion.

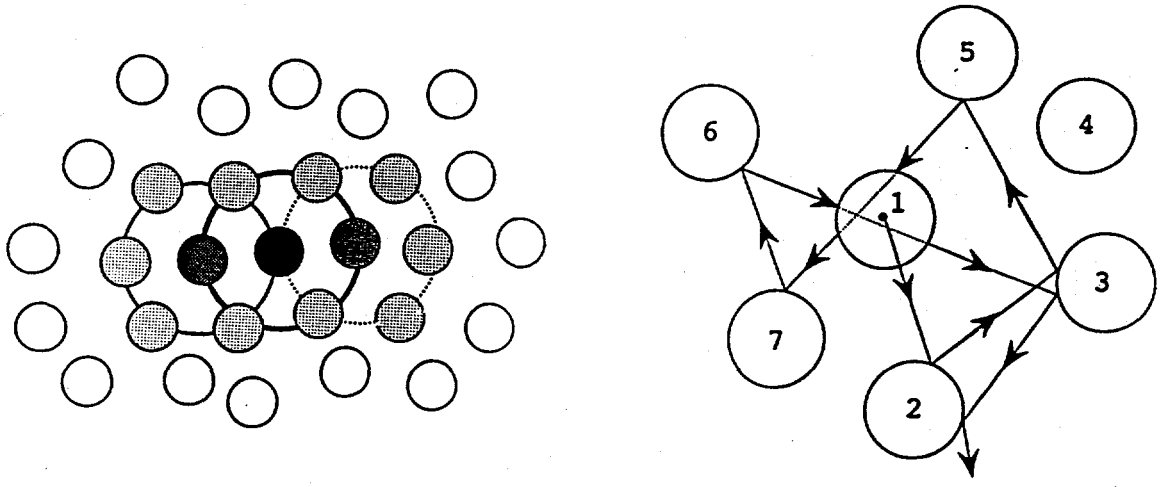

Figure 2. (a) The central particle (black) is in a cage whose wall is formed by the particles connected by the thick black line. Each wall particle is itself the center of a cage, of which the black particle is part of the wall. This is illustrated for two wall particles of the black particle, for which the cage walls are formed by particles connected by a solid line or a dotted line, respectively; (b) cage diffusion collisions of central particle 1 for fixed wall particles 2 to 7. The interparticle distances have been considerably enlarged for clarity.

The high frequency part $\eta^{\text{eff}}_{\infty}(\phi)$ of $\eta^{\text{eff}}(\phi;\omega)$ has been studied experimentally by a variety of methods and the expression (4) is in very good agreement with experiment for all $0 < \phi < 0.55$ (cf.fig.3). The physical interpretation of (4) is that for very short times, even smaller than the (Brownian) time $t_B = \sigma^2/4\nu_s \approx 10^{-7}$ sec, where ν_s is the kinematic viscosity of the solvent, the suspension viscosity is determined not only by that of the pure solvent viscosity η_s, but also by a correction factor $\chi(\phi)$ which gives the increase in effective suspension viscosity due to the pairs of touching ($r = \sigma$) particles present in the suspension. This is a very short time contribution to $\eta^{\text{eff}}(\phi;\omega)$, due to statistical thermodynamic, (i.e., hard sphere excluded volume) interactions, arising from the canonical equilibrium distribution of the colloidal particles, rather than the usually considered hydrodynamic interaction contributions. The time scale of the contributions of the second term in (3) is much longer than that of the first term and is related to the time scale on which the cage diffusion takes place, viz., the Péclet time $t_P = \sigma^2/4D_0 \approx 10^{-3}$ sec.

For $\omega = 0$, one obtains then from (3) for the effective Newtonian viscosity $\eta^{\text{eff}}(\phi) \equiv \eta^{\text{eff}}(\phi;0)$ of the suspension, with (2), the simple expression:

$$\eta^{\text{eff}}(\phi) = \eta_s \chi(\phi)[1 + \frac{1}{40\pi}\int_0^{\infty} d\kappa \frac{\kappa^2 [S'_{eq}(\kappa;\phi)]^2}{d(\kappa) S_{eq}(\kappa;\phi)}] \quad (5)$$

with $\kappa = k\sigma$.

Although this expression for $\eta^{\rm eff}(\phi)$ has been derived for large ϕ $(0.3 < \phi < 0.55)$ it is also applicable to small $\phi < 0.3$, since the second term in the square brackets mainly contributes for $\phi > 0.3$ and the first term $\eta_s\chi(\phi)$ adequately describes the smaller ϕ behavior (cf.fig.5).

For $\omega \neq 0$, one obtains the effective visco-elastic behavior of the suspension. Since $\eta^{\rm eff}(\phi;\omega)$ is complex one can consider its real and imaginary parts $\eta^{\rm eff}(\phi;\omega) = \eta_R^{\rm eff}(\phi;\omega) - i\eta_I^{\rm eff}(\phi;\omega)$ or equivalently those of $\eta^*(\phi;\omega) = [\eta^{\rm eff}(\phi;\omega) - \eta^{\rm eff}(\phi;\infty)]/[\eta^{\rm eff}(\phi;0) - \eta^{\rm eff}(\phi;\infty)]$, where $\eta^{\rm eff}(\phi;\infty) \equiv \eta_\infty^{\rm eff}(\phi)$, used before. In fig.6 they are plotted as a function of ω and compared with experiment[8,9]. They show a virtual absence of any concentration dependence within the spread of the experimental data. The theoretical asymptotic large ω behavior $\sim (\omega\tau_P)^{-1/2}$ for all ϕ, is consistent with what is found experimentally.

Discussion

We conclude with a number of remarks.

1. The Newtonian viscosity of a colloidal suspension in the fluid phase $0 < \phi < 0.55$ can be obtained without adjustable parameters for all concentrations from eq.(5). All that is needed, apart from D_0, is the hard sphere diameter σ to define the system. This can be obtained directly from electron microscopy or, for concentrated suspensions, from the first sharp maximum of $S_{eq}(k;\phi)$[4,7].
2. The good agreement between theory (eq.(5)) and experiment (figs.3,5), appears to confirm the correctness of the two basic physical mechanisms, which are at the heart of the eq.(5): statistical thermodynamic forces for very short times $(\leq t_B)$ and cage diffusion for longer times $(\geq t_P)$.
3. Hydrodynamic interactions are relevant on a time scale $\gg t_B$, but their effect is not detectable on the scale on which $\eta^{\rm eff}(\phi)$ is plotted in fig.5, where an almost hundred-fold increase of the effective viscosity of the suspension occurs over the fluid range $0 < \phi < 0.55$. They are surely present (cf.fig.3), but relatively small at small ϕ and appear to be quenched at large ϕ.
4. This leads to the prediction that the same behavior for $\eta^{\rm eff}(\phi)$ and $\eta^{\rm eff}(\phi,\omega)$ will be observed for *charged* colloidal suspensions, at least at large $\phi > 0.3$, if (a) one identifies the hard sphere diameter σ with the *Debye sphere diameter* and (b) ω is not such that deformations of the Debye spheres are relevant.

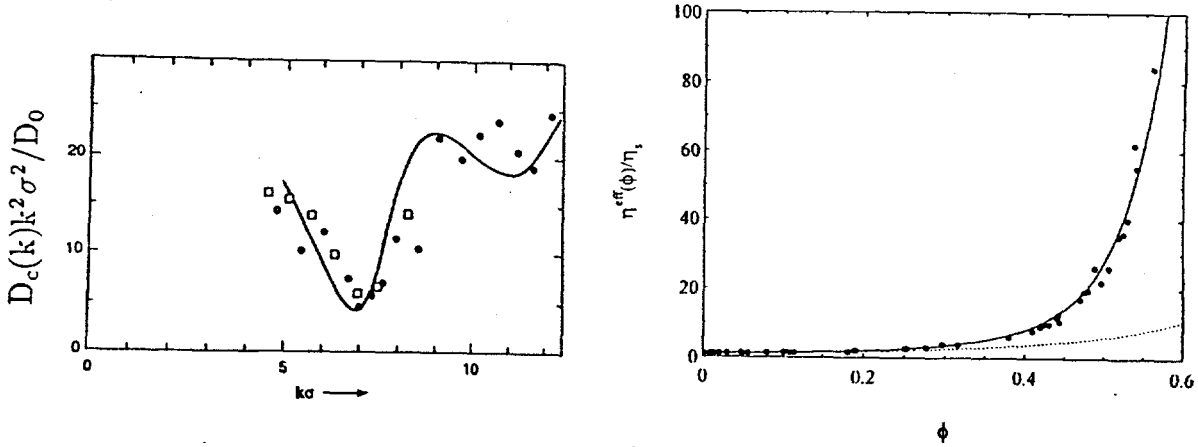

Figure 4 (left). Reduced cage diffusion coefficient $D_c(k)k^2\sigma^2/D_0$ as function of $k\sigma$ from light scattering for a charged colloid (closed circles; Ref.8(a), $\sigma = 600$nm, $\phi = 0.48$), a neutral colloid (open squares; Ref.8(b), $\sigma = 335$nm, $\phi = 0.49$) and from theory (solid line; Eq.(2)). The two minima correspond to the first two maxima of $S(k)$.
Figure 5 (right). Reduced Newtonian viscosity $\eta^{\rm eff}(\phi)/\eta_s$ as a function of ϕ from experiment (closed circles, Ref.10) and theory (solid line, cf.Eq.(5)). The dashed curve is $\chi(\phi)$.

5. For the very high frequency behavior $\eta_\infty^{\rm eff}(\phi)$ an Einstein relation holds for all $0 < \phi < 0.55$:

$$\eta_\infty^{\rm eff}(\phi) = \frac{k_B T}{6\pi D_s^{\rm eff}(\phi)(\sigma/2)} \tag{6}$$

Here $D_s^{\rm eff}(\phi)$ is the (effective) self-diffusion coefficient of the colloidal suspension at volume fraction ϕ, i.e., the diffusion coefficient of a tagged colloidal particle with respect to the other (identical) colloidal particles. In so far as $D_s^{\rm eff}(\phi)$ can be measured by light scattering techniques[8,9], $D_s^{\rm eff}(\phi)$, which characterizes the diffusive decay of density fluctuations, allows a non-mechanical determination of $\eta_\infty^{\rm eff}(\phi)$. Together with the usual Einstein relation and eq.(4),(6) leads to: $\eta_\infty^{\rm eff}(\phi)/\eta_s = D_0/D_s^{\rm eff}(\phi) = \chi(\phi)$ (cf.fig.4).

The physical origin of the validity of (6) is the inert character of the suspension surrounding two touching particles, at high frequencies, i.e., at very short times.

6. For large $\phi > 0.3$ an expression for the Newtonian viscosity of an atomic liquid very similar to (3) for $\omega = 0$, has been derived. This illustrates a close physical analogy of concentrated colloidal suspensions consisting of spherical particles on the one hand and simple atomic liquids, like liquid argon or liquid methane, on the other hand[4,7,12]. This analogy is based on a similarity of both fluid systems to dense hard sphere fluids, a similarity used above (in section 2) to obtain the crucial relation (2) for the colloidal suspension. The physical origin of this similarity is based on (a) the similarity of Brownian and Newtonian motion on large time scales ($t \gg t_B$)[13] and (b) the similarity of the cage-diffusion process in the two fluid systems. For further details we refer to the literature[4,12].

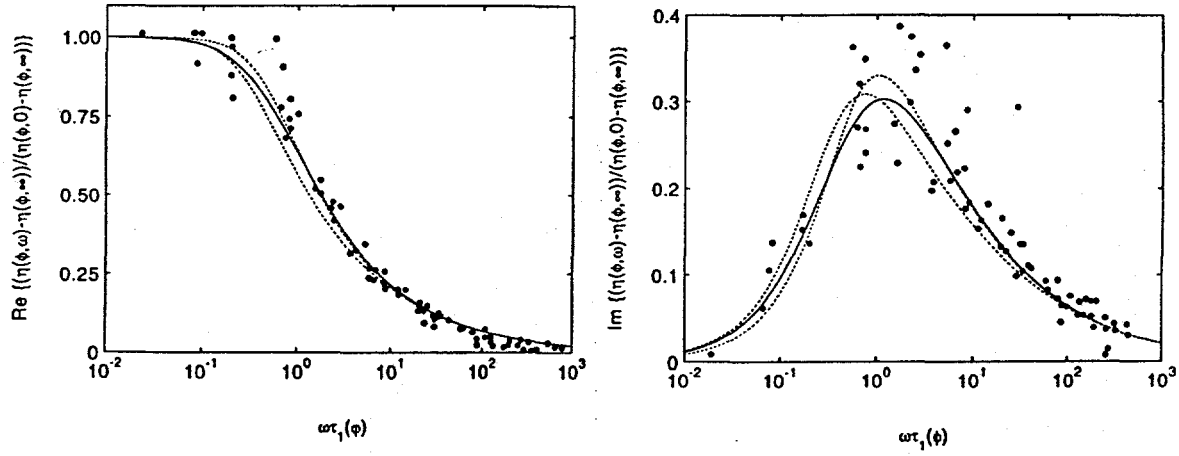

Figure 6. Real part (a) and imaginary part (b) of the reduced complex shear viscosity $\eta^*(\phi,\omega)$, as a function of reduced frequency $\omega\tau_1(\phi)$ (with $\tau_1(\phi) \approx \tau_P/4$ cf.Ref.1). The closed circles are from Ref.10. The dashed curves are from Eq. 3 for $\phi = 0.4$ and 0.5 (from left to right, respectively). The solid curve, for $\phi = 0$, is exact and from Ref.11.

ACKNOWLEDGEMENT

One of us (EGDC) is indebted to the Department of Energy grant number DE-FG 02-88-ER13847 for financial support.

REFERENCES

[1]. I. M. DE SCHEPPER, H. E. SMORENBURG and E. G. D. COHEN, *Phys. Rev. Lett.* 70, 2178 (1993).

[2]. I. M. DE SCHEPPER and E. G. D. COHEN, *Int. J. of Thermod.* 15, 1179 (1994).
[3]. D. HENDERSON and E. W. GRUNDKE, *J. Chem. Phys.* 63, 601 (1975).
[4]. E. G. D. COHEN and I. M. DE SCHEPPER, *Recent Progress in Many-Body Theories 3*, ed. T. L. Ainsworth, C. E. Campbell, B. E. Clements, and E. Krotscheck, (Plenum, New York, 1992) p. 387; *Slow Dynamics in Condensed Matter*, First Tohwa University International Symposium, Fukuoka, Japan, ed. K. Kawasaki, T. Kawaskatsu and M. Tokuyama (American Institute of Physics, New York, 1992) p. 359.
[5]. I. M. DE SCHEPPER, E. G. D. COHEN and H. J. ZUILHOF, *Phys. Lett. A*101, 399 (1984).
[6]. E. G. D. COHEN and I. M. DE SCHEPPER, *J. Stat. Phys.* 63, 241, 419 (1991).
[7]. I. M. DE SCHEPPER, E. G. D. COHEN, P. N. PUSEY and H. N. W. LEKKERKERKER, *J. Phys. Condens. Matter* 1, 6503 (1989); P. N. PUSEY, H. N. W. LEKKERKERKER, E. G. D. COHEN and I. M. DE SCHEPPER, *Physica A*164, 12 (1990).
[8]. (a) T. W. TAYLOR and B. J. ACKERSON, *J. Chem. Phys.*, 83, 2441 (1985); (b) P. N. PUSEY and W. VAN MEGEN, *Phys. Rev. Lett.* 59, 2083 (1987).
[9]. (a) J. X. ZHU, D. J. DURIAN, J. MÜLLER, D. A. WEITZ, and D. J. PINE, *Phys. Rev. Lett.* 68, 2559 (1992); (b) W. VAN MEGEN, S. M. UNDERWOOD, R. H. OTTEWILL, N. WILLIAMS and P.N. PUSEY, *Faraday Discuss. Chem. Soc.*, 83, 47 (1987).
[10]. J. C. VAN DER WERFF, C. G. DE KRUIF, C. BLOM and J. MELLEMA, *Phys. Rev. A*39, 795 (1989); J. C. VAN DER WERFF and C. G. DE KRUIF, *J. Rheol.* 33, 421 (1989).
[11]. B. CICHOCKI and B. U. FELDERHOF, *Phys. Rev. A*43, 5405 (1989).
[12]. E. G. D. COHEN, *Physica A*194, 229 (1993); id., *Twenty-five Years of Non-Equilibrium Statistical Mechanics*, XIII Sitges Conference, *Lecture Notes in Physics*, Springer (1995).
[13]. H. LÖWEN, J. P. HANSEN and J. N. ROUX, *Phys. Rev. A* 44, 1169 (1991).

GELATION UNDER SHEAR[1]

B.D. Butler, H.J.M. Hanley, and G.C. Straty

Thermophysics Division
National Institute of Standards and Technology
Boulder, Colorado, 80303, U.S.A

C.D. Muzny

Department of Physics, University of Colorado
Boulder, Colorado, 80309, U.S.A.

ABSTRACT

An experimental small angle neutron scattering (SANS) study of dense silica gels, prepared from suspensions of 24 nm colloidal silica particles at several volume fractions ϕ is discussed. Provided that $\phi \lesssim 0.18$, the scattered intensity at small wave vectors q increases as the gelation proceeds, and the structure factor $S(q,t \to \infty)$ of the gel exhibits apparent power law behavior. Power law behavior is also observed, even for samples with $\phi > 0.18$, when the gel is formed under an applied shear. Shear also enhances the diffraction maximum corresponding to the inter-particle contact distance of the gel. Difficulties encountered when trying to interpret SANS data from these dense systems are outlined. Results of computer simulations intended to mimic gel formation, including computations of $S(q,t)$, are discussed. Comments on a method to extract a fractal dimension characterizing the gel are included.

INTRODUCTION

The gelation of silica is of current interest both because gelation contains some interesting physics and because silica gel technology is an essential factor in the preparation and fabrication of modern ceramic materials [1]. A theme which has driven progress in the understanding and subsequent improvement in design of many material systems is the relationship between the properties of materials (mechanical, thermal, electrical, etc.) and their structure. Surprisingly, structural studies are relatively rare in the technologically relevant dense gels. This paper

[1] Contribution of the National Institute of Standards and Technology, not subject to copyright in the U.S.

summarizes some small angle neutron scattering (SANS) data which help to interpret the structural changes that take place during the gelation of silica. Specifically, the motivation was to understand better the evolution of the structure, on mesoscopic scales, of dense gelling silica spheres both with and without the influence of an applied shear. We report on: (1) the evolution of the structure factor in a gelling silica suspension (sol) subjected to an applied shear and compare this to similar systems without shear; and (2) the methods we use to interpret SANS data from *dense* gelling systems.

Experiments to probe the influence of shear on these systems are novel, but we anticipate that shear will impact the structure and formation mechanism of gels. Consider a gel as a mechanically and thermodynamically unstable microscopic network made up of some defined unit, for example, a particle or segment of a polymer chain. Instability is frozen when the network growth and/or rearrangement is restricted by the finite size of the container and the experimental conditions [2]. It is, however, known [3] that a shear rate γ applied to a system will affect its equation of state, its thermodynamic properties, and therefore its phase stability criteria. Thus, a sheared system may have phase behavior which is perturbed or even qualitatively different from its counterpart formed in isolation. Since gelation can be treated as a phase change, a shear applied to the precursor or sol can be expected to influence the final gel structure.

EXPERIMENT

This study [4] was carried out with colloidal silica particles, of nominal diameter $\sigma = 24$ nm, on the 30 m SANS instruments at the NIST Cold Neutron Research Facility. Silica spheres were suspended in a 70% H_2O - 30% D_2O medium (to reduce the effect of multiple scattering) at volume fractions ϕ of 0.10, 0.12, 0.18, 0.24, and 0.30. Gelation was initiated by lowering the pH of the suspensions to 5.8 ± 0.1 with the addition of 0.1M HCl. For gelation to proceed at a reasonable pace, NaCl was added to some designated samples until the solutions reached 0.4M NaCl.

The samples were placed in quartz cells of path length 1 mm, and the spectrometer was configured to an incident wavelength of 0.6 nm at a detector distance of 13 m. The scattered intensity was measured using a 2D position sensitive detector system, and, since asymmetry was not observed in any of the samples, the detector counts were averaged azimuthally. The measured scattered intensities were corrected for cell background and detector efficiency and were placed on an absolute scale by normalizing to the scattering from an appropriate standard. The structure factor was obtained by dividing this normalized intensity by a theoretical polydisperse form factor [4] modified to allow for instrument smearing. Data were collected after gel initiation at 10 min intervals for the first 3 h and then hourly until gelation was complete. Gelation was considered complete when the measured intensity became time independent (usually after 6-10 h).

For the shear studies, the SANS instrument was configured at 13 m and 8 m at a wavelength of 0.6 nm with the NIST 0.5 mm gap-width Couette shearing cell [5] in the sample holder position with the incident beam perpendicular to the flow direction. A gelation-initiated sample was loaded into the Couette cell, subjected to a shear rate $\gamma = 4500\ s^{-1}$, and the intensity recorded. A sector average of the sheared intensities indicated possible weak anisotropy at the higher volume fractions, but the data were circularly averaged and reduced following the procedure for the unsheared suspensions and gels. Intensities were measured at regular intervals until the scattering pattern from the shearing system was time-independent. At this point the shear was removed and

the intensity remeasured. Only very small relaxation was noted; in effect, the intensity did not change significantly when the shear was removed.

RESULTS

The presentation of these results and their interpretation is a distillation of the discussions of our work reported in Refs. [4, 6-8]. The data are summarized in Figures 1 and 2. Figure 1 (a) shows a typical sequence of the variation of the structure factor $S(q,t)$ as a function of time after gel initiation for a $\phi = 0.10$ sample gelling in the absence of an applied shear. At the very earliest times there is no appreciable small angle scattering, indicating the initial solution is relatively homogeneous at the length scales probed by this experiment (several particle diameters). As the gelation proceeds, however, there is a marked increase in the scattering at low q and this becomes more pronounced at longer times. At these later times, $S(q,t)$ displays an apparent power-law increase with decreasing q. Behavior qualitatively similar to this was observed in all samples, sheared and unsheared, that had silica volume fractions $\phi \leq 0.18$, with the lowest volume fractions showing the most intense small angle scattering. Quantitative differences between the samples with $\phi \leq 0.18$ measured with and without an applied shear were small.

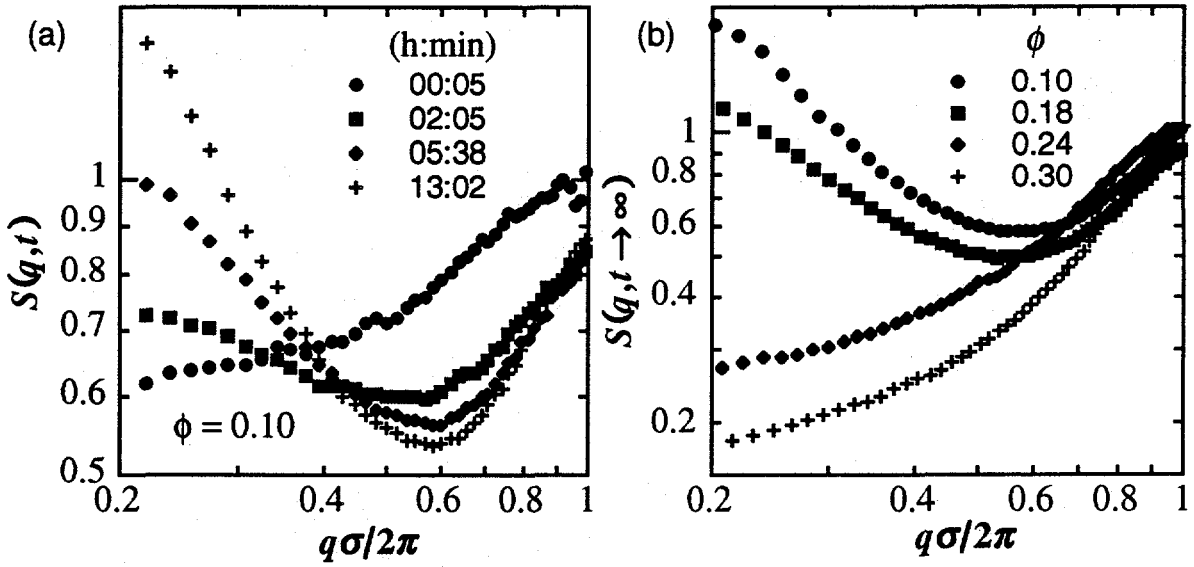

Figure 1: Measurered structure factors at $\gamma = 0$: (a) as a function of time since gel initiation, and (b), as a function of volume fraction after the gel has formed.

In contrast, samples with silica volume fractions above 0.18 ($\phi = 0.24,\ 0.30$) did not display a rise in the small angle scattering (even at very long times) when a shear was not applied. This result is apparent from Fig. 1 (b), which shows the scattering from the final gels as a function of volume fraction. Thus, the power-law increase in the scattering at small angles observed in the more dilute systems is not seen in the denser system. This power-law behavior in $S(q,t)$ returns, however, when shear is applied during the gelation of the higher density samples (Fig. 2). Furthermore, in addition to this large increase in small angle scattering with shear, there is a significant change observed in the particle-particle 'contact' peak located near $q\sigma/2\pi \approx 1$. This peak is broad and weak in the unsheared sample, but is much sharper and more intense in the sample gelled under shear.

Qualitatively, the increase in small angle scattering at low q indicates that the samples evolve from an initially homogeneous suspension of silica particles to an arrangement that contains structural inhomogeneities at length scales of the order of several particle diameters. These inhomogeneities apparently do not form at all in samples with volume fractions greater than 0.18 unless a shear is applied. This is a surprising result. We might anticipate that a shear will disorder the gel so as to prevent the formation of inhomogeneities; apparently the opposite is true. Moreover, the distinct particle-particle contact peak seen in the higher density sheared gels (Fig. 2) indicates that relatively dense clusters of these spherical silica particles have formed.

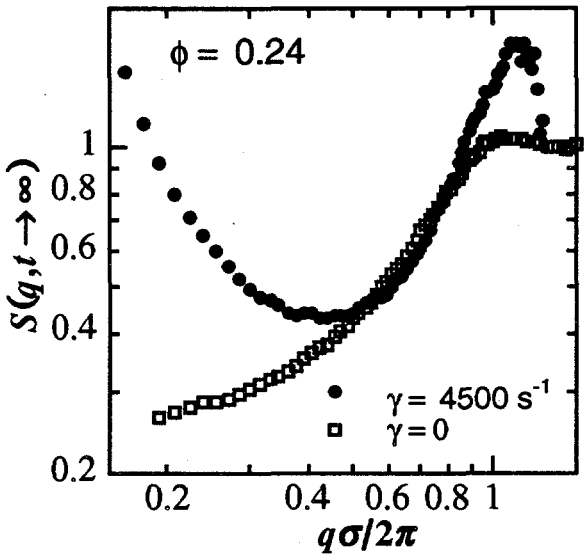

Figure 2: Measurered structure factors for the $\phi = 0.24$ gelled samples with and without an applied shear. The results for $\phi = 0.30$ are similar.

ANALYSIS

In *low* density gels, small angle x-ray [9], neutron [10], and light-scattering [11] studies show a characteristic power-law increase in intensity with decreasing wavevector. This power-law behavior, characteristic of fractal aggregation processes [12, 13], predicts that the mass of an aggregate varies as $m \sim \xi^{d_f}$, where ξ is a length characterizing the aggregate size and d_f is a fractal dimension. It is easily shown that the structure factor $S(q)$ of a collection of such objects is given by

$$S(q) \sim q^{-d_f} \tag{1}$$

at wavevectors in the range $2\pi/\xi << q << 2\pi/\sigma$, *provided* that there are no correlations between aggregates. The power-law slopes in the measured small-angle diffraction patterns of these low density gels (where correlations can be expected to be small) are thus related to the fractal dimension of the aggregates that form the gel.

It is tempting to apply Eq. (1) to our data and derive a fractal dimension from the slope of the measured structure factors. But, in this study, the small angle neutron scattering measurements

were performed on dense gels for which an assumption that the collection of aggregates or clusters of particles formed during gelation are uncorrelated *cannot* be justified. In these dense systems, the small angle scattering can be described only by a much more complicated function of the cluster shapes, cluster-cluster correlations, as well as the particle arrangements inside individual clusters [7]. Cluster growth and/or cluster-cluster correlations must, therefore, be included in the interpretation of the increased scattering at low angles. In other words, it is not necessarily the internal arrangements of the silica particles inside a cluster that cause the rise in scattering as it is in low density systems; rather, the size and shape of the clusters coupled with their correlation must be a factor.

COMPUTER SIMULATION

The direct interpretation of such complicated scattering patterns requires that we evoke some model of the particle rearrangement. We chose to simulate the gelation in a dense 2D system where it is possible both to observe the particle positions as a function of time and to compare this to an $S(q,t)$ computed from these configurations. In this way it is possible to gain insight into how cluster morphologies contribute to particular features of the corresponding diffraction patterns and therefore be better able to interpret the measurements. Furthermore, it is possible to simulate the effect of shear on the particle morphologies, and thus $S(q,t)$, and to compare this to our scattering measurements.

Details of the computer simulation are presented elsewhere [6], but, in brief, it consisted of quenching (by molecular dynamics methods) a large (N = 14336), dense (ρ = 0.325), 2D Lennard-Jones system, from a high temperature disordered fluid into the vapor/solid coexistence region and observing the subsequent aggregation both with and without an applied shear. The quench is intended to mimic the sudden change in interaction potential used to initiate gelation in real systems – the subsequent evolution of the real and simulated systems should therefore be qualitatively similar. In order to compare these simulations to experiment, $S(q,t)$ was computed from the simulation and compared with the experimental data and the simulated particle morphologies. Typical results from the simulations are presented in Fig. 3.

Figures 3 (a) and (b) are taken from a simulation with no applied shear after a total reduced time t = 500 since the quench. At this relatively late stage in the evolution of the system several large clusters with elongated shapes have formed which, overall, shows an interconnected morphology. Most interesting for our present purposes is the form of the computed $S(q,t)$. Like the experiments reported earlier, $S(q,t)$ shows a power-law-like rise with decreasing wavevector, but, in this case, the origin of the small angle scattering in the simulation is clear; there is a peak in $S(q,t)$ at low angles which results from the cluster-cluster correlations evident in Fig. 3 (a). The power-law slope cannot be identified with any particular internal feature of the clusters but instead depends on specific details of the correlations which give rise to the peak in $S(q,t)$.

Similar plots after the same time are presented in Figs. 3 (c) and (d) for the case where a shear is applied. Here we find that the coarsening of the clusters has proceeded much more rapidly than in the simulation where no shear was applied. While this might not be expected, as we may anticipate that shear will *disorder* the system, it is consistent with our experimental observation that the application of a shear in the dense gels gives rise to small angle scattering where none is present in the unsheared gels.

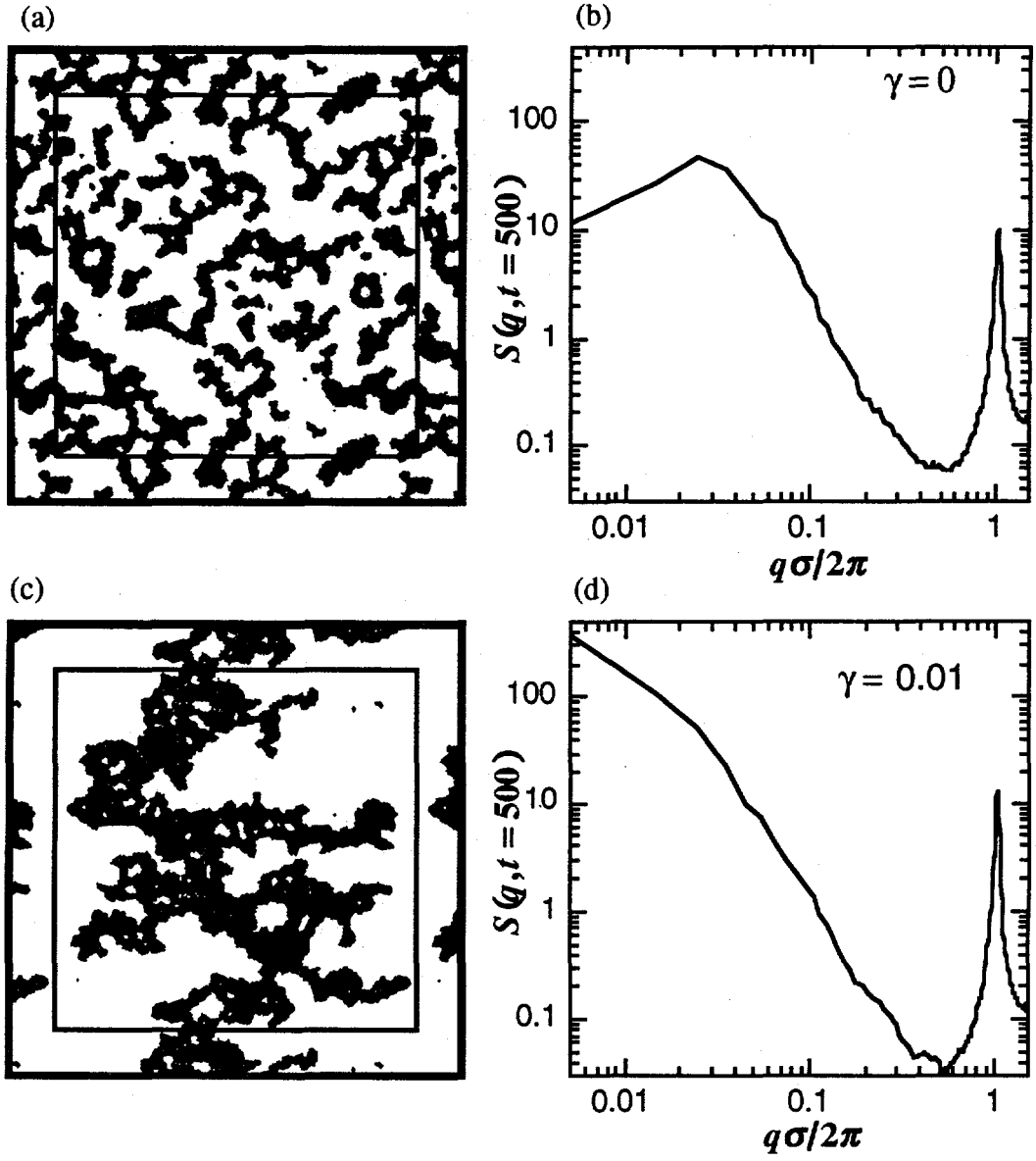

Figure 3: Molecular dynamics computer simulations of quenched Lennard-Jones disks: (a) and (c) are particle configurations at a reduced time $t = 500$ without and with an applied shear; (b) and (d) are the corresponding $S(q)$.

A DYNAMIC SCALING LAW

Close examination of the evolution of the cluster morphology showed that the aggregation proceeds in such a way that, except for a change in scale, the morphologies are similar. That is, the structure evolves in a temporally self-similar manner. If the clusters are mass fractals, the corresponding structure factors should, therefore, scale as [8]

$$S(q/q_m(t)) \sim q_m(t)^{-d_f} \tilde{S}(q/\tilde{q}_m) \tag{2}$$

where $q_m(t)$ is the location of the low angle peak in $S(q,t)$ and $\tilde{S}(q/\tilde{q}_m)$ is a time-independent characteristic structure function which peaks at $\tilde{q}_m$. The fractal dimension d_f is allowed to take on any value less than or equal to the dimensionality of the system and will depend on the structure of the evolving clusters. For the simulations presented here, this relation is satisfied well provided d_f is assigned a value of 1.85 ± 0.05. This result is presented in Fig. 4. Here the computed $S(q,t)$ have been scaled according to Eq. 2 and are found to lie on a universal curve. This result is important because it suggests a way to obtain information (the fractal dimension) about the structure of the evolving system, even in a dense system where correlations are inevitable, by observing the time dependence of the structure factor.

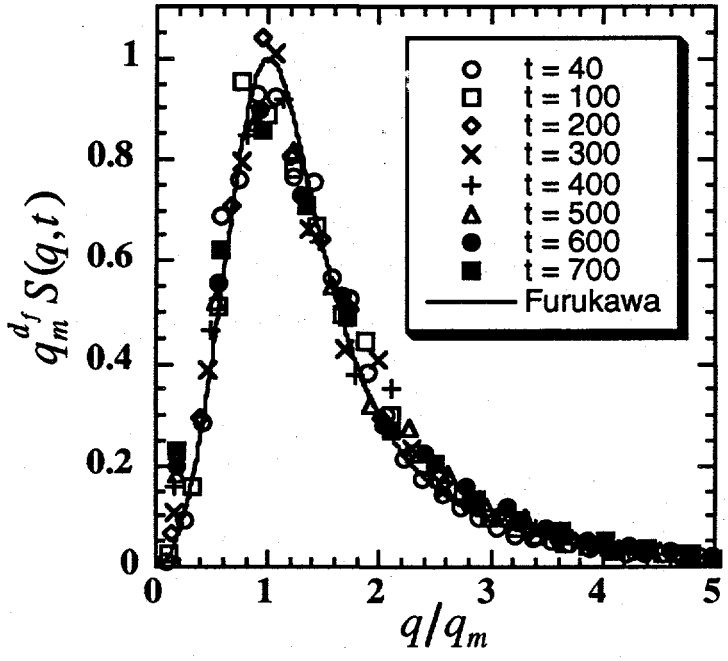

Figure 4: Computed stucture factors at different times during the evolution of the MD computer simulation (no shear) scaled according to Eq. (2). The solid line is the phenomenological theory of Furukawa [14] which has no adjustable parameters. See Ref. [8].

CONCLUSION

Measurement of SANS data on silica gels ranging in volume fraction ϕ from 0.10 to 0.30, were made with and without an applied shear. Those samples with $\phi \leq 0.18$ showed apparent power-law increases in their structure factors regardless of shear. The two higher density samples only displayed power-law rises in $S(q,t)$ when a shear was applied, indicating that shear actually assists the gelation processes that operate at lower density. A computer model based on the quenching of a Leonard-Jones system reproduces many features of the measured diffraction data – a power-law behavior and an increased tendency for ordering when a shear is applied. Comparing the simulation results with the data, we conclude that the power law behavior originates from the presence of cluster-cluster correlations and not from the internal fractal structure of these clusters. We present a dynamic scaling relation which can instead be used to derive the fractal dimension of

the evolving system even in the presence of these correlations.

ACKNOWLEDGEMENTS

This work was supported in part by a grant from the Office of Basic Energy Sciences, Division of Engineering and Geosciences, US Department of Energy. BDB was supported by a National Research Council Research Associateship. We are grateful to William O. Roberts, Du Pont, for supplying the silica samples and for valuable discussions. Part of the neutron studies were carried out on the NIST SANS instrument supported by the National Science Foundation under Agreement No. DMR-9122444.

REFERENCES

1. See, for example, C.J. Brinker and G.W. Scherer, *Sol-Gel Science: The Physics and Chemistry of Sol-Gel Processing*, Academic, San Diego (1990).
2. Experiment supports this view, for example; (a) a suspension can be gelled very slowly giving either an amorphous liquid-like solid phase (as for a slowly dried silica gel) or a crystal (as in opal formation); (b) on aging, a gel can rearrange to a metastable amorphous solid or to a stable crystal (See Ref. [1]).
3. H.J.M. Hanley and D.J. Evans, J. Chem. Phys. 76, 3225 (1982).
4. C.D. Muzny, G.C. Straty and H.J.M. Hanley, Phys. Rev. E. 50, R675 (1994).
5. G.C. Straty, H.J.M. Hanley, and C.J. Glinka, J. Stat. Phys. 62, 1015 (1991).
6. C. D. Muzny, D. Hansen, G, C,. Straty, D. J. Evans and H. J. M. Hanley, Simulation and SANS studies of gelation under shear, *Int. J. Thermophysics*, 16, 337 (1995).
7. B.D. Butler, H.J.M. Hanley, C.D. Muzny and G.C. Straty, Mat. Res. Soc. Symp. Proc., *Neutron Scattering in Materials Science* 376, *in press*.
8. B.D. Butler, H.J.M. Hanley, D. Hansen and D.J. Evans, Phys. Rev. Lett., *in press* (1995).
9. D.W. Schaefer, J.E. Martin, P. Wiltzius, and D.S. Cannell, *Phys. Rev. Lett.* **52**, 2371 (1984).
10. R. Vacher, T. Woignier, J. Pelous, and E. Courtens, *Phys. Rev. B* **37**, 6500 (1988).
11. G. Dietler, C. Aubert, D.S. Cannell, and P. Wiltzius, *Phys. Rev. Lett.* **57**, 3117 (1986).
12. P. Meakin, *Ann. Rev. Phys. Chem.* **39**, 237 (1988).
13. J. E. Martin and B.J. Ackerson, *Phys. Rev. A* **31**, 1180 (1985).
14. H. Furukawa, Adv. Phys. 34, 703 (1985).

TRANSPORT PROPERTIES OF POROUS MEDIA FROM THE MICROSTRUCTURE

S. Torquato

Department of Civil Engineering & Operations Research and Princeton Materials Institute
Princeton University, Princeton, N.J. 08544

ABSTRACT

The determination of the effective transport properties of a random porous medium remains a challenging area of research because the properties depend on the microstructure in a highly complex fashion. This paper reviews recent theoretical and experimental progress that we have made on various aspects of this problem. A unified approach is taken to characterize the microstructure and the seemingly disparate properties of the medium.

I. INTRODUCTION

The purpose of this paper is to review progress that we have made in the last several years on five basic aspects of the problem of determining effective transport properties of random porous media: (i) derivation of rigorous bounds on transport properties in terms of statistical correlation functions; (ii) quantitative characterization of the microstructure of nontrivial models; (iii) 3D imaging of porous media using x-ray tomography; (iv) and derivation of rigorous cross-property relations.

II. AVERAGED EQUATIONS

The random porous medium is a domain of space $\mathcal{V}(\omega) \in \boldsymbol{R}^3$ (where the realization $\boldsymbol{\Omega}$ is taken from some probability space ω) of volume V which is composed of two regions: the pore region $\mathcal{V}_1(\omega)$ (in which transport occurs) of volume fraction (porosity) ϕ_1 and a solid-phase region $\mathcal{V}_2(\omega)$ of volume fraction ϕ_2. Let $\partial\mathcal{V}(\omega)$ be the surface between $\mathcal{V}_1$ and $\mathcal{V}_2$.

A. Time Scales for NMR Relaxation

Nuclear magnetic resonance (NMR) is a powerful noninvasive technique for the study of fluid-saturated porous media [1]. The relaxation times of water contained in a porous medium are substantially smaller than those of bulk water, primarily because of enhanced

relaxation mechanisms at the pore-solid interface. NMR relaxation depends upon the characteristic length scales of the pore space and on the surface rate constant κ. The decay of the magnetization density $m(\mathbf{x},t)$ at local position $\mathbf{x}$ and time t is governed by a time-dependent diffusion equation, the solution of which can be expressed as an expansion in orthonormal eigenfunctions $\{\psi_n\}$:

$$\frac{m(\mathbf{x},t)}{m_o} = \sum_{n=1}^{\infty} a_n e^{-t/T_n} \psi_n(\mathbf{x}) \,, \tag{1}$$

where the coefficients a_n are simply related to the pore-volume average of ψ_n [2]. The diffusion relaxation times T_n are inversely proportional to the eigenvalues λ_n.

The net magnetization, usually the quantity of principal interest in NMR experiments, is defined as

$$M(t) = \int_{\mathcal{V}_1} m(\mathbf{x},t) d\mathbf{x} \,. \tag{2}$$

The *mean survival time* τ of a diffusing particle before it gets completely demagnetized is given by [2]

$$\tau = \int_0^{\infty} \frac{M(t)}{M_o} dt, \tag{3}$$

where $M_o \equiv M(t=0)$. The mean survival time τ depends on the diffusion coeffcient, D, κ, and the microstructure.

B. Effective Conductivity

The effective conductivity σ_e is given by an averaged Ohm's law:

$$< \mathbf{J}(\mathbf{x}) >= \sigma_e < \mathbf{E}(\mathbf{x}) > \tag{4}$$

where $< \mathbf{E}(\mathbf{x}) >$ and $< \mathbf{J}(\mathbf{x}) >$ represent the *ensemble average* of the local electric and current density fields, respectively. The local fields satisfy the usual steady-state conduction equations [3].

By mathematical analogy, results for σ_e translate into equivalent results for the thermal conductivity, magnetic permeability, dielectric constant, and diffusion coefficient.

C. Fluid Permeability

The fluid permeabilty k of a porous medium, defined by Darcy's law,

$$< \mathbf{u}(\mathbf{x}) >= -\frac{k}{\mu} \nabla p_o(\mathbf{x}) \,, \tag{5}$$

governs the rate at which a viscous fluid flows through it [4]. Here $< \mathbf{u}(\mathbf{x}) >$ is the ensemble average of the local fluid velocity which satisfies the steady-state Stokes equations [5], $\nabla p_o(\mathbf{x})$ is the applied pressure gradient, and μ is the dynamic viscosity. k depends nontrivially on the pore geometry and may be regarded to be an *effective cross-sectional area of pore channels.*

III. MICROSTRUCTURE/PROPERTY CONNECTION

A. Minimum Energy Principles

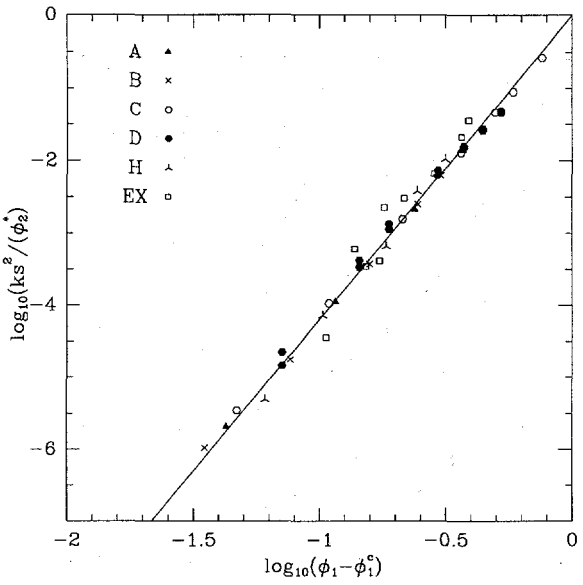

Figure 1: The log of $ks^2/2\phi_2$ vs. log of $\phi_1 - \phi_1^c$ for several different model microstructures and a sandstone. Here s is the specfic surface and ϕ_1^c is the porosity at which the pore phase becomes disconnected.

For general random media, the complexity of the microstructure prevents one from obtaining the effective properties of the system exactly. Therefore, any rigorous statement about the properties must be in the form of an inequality, i.e., rigorous bounds on the effective properties. Bounds are useful since they: (i) enable one to test the merits of theories and computer experiments; (ii) as successfully more microstructural information is incorporated, the bounds become progressively narrower; and (iii) one of the bounds can typically provide a good estimate of the property for a wide range of conditions, even when the reciprocal bound diverges from it.

Bounds are usually derived using *minimum energy principles* [3]. Recently, the mean survival time τ has been bounded from below in terms of moments of the *pore size distribution function* $P(\delta)$ [2,6]. $P(\delta)\,d\delta$ is the probability that a point in the pore region $\mathcal{V}_1$ lies at a distance between δ and $\delta + d\delta$ from the nearest point on the interface $\partial\mathcal{V}$.

The nearest-neighbor distribution function $H(r)$ has been shown to arise in rigorous bounds on the effective conductivity σ_e, mean survival time τ, and the fluild permeability k for suspensions of spheres [6]. $H(r)\,dr$ gives the probability of finding nearest neighbors in a spherical shell of thickness dr at a distance r from the center of a reference particle.

More recently, we have derived the sharpest available bounds on the effective conductivity and elastic moduli of two-phase heterogeneous materials that are given in terms of the n-point probability functions S_1, S_2,..., S_n [7]. $S_n(\mathbf{r}_1, ..., \mathbf{r}_n)$ gives the probability of finding n point at positions $\mathbf{r}_1$,...,$\mathbf{r}_n$ in one of the phases.

Guided by rigorous bounds on the permeability, we have found a universal scaling for the permeability of a class of porous media [8]. As Figure 1 demonstrates this includes various sphere packings as well as a sandstone.

B. Brownian-Motion Simulation Technique

We have applied our Brownian-motion simulation technique to compute effective diffusion properties, such as the effective conductivity of packings of spheroids [9] and mean survival time associated with diffusion-controlled reactions in *digitized, synthetic* heteroge-

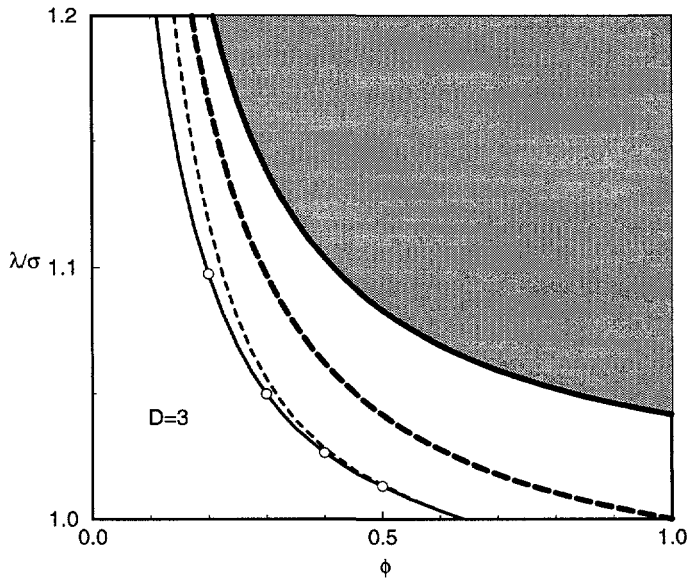

Figure 2: Dimensionless mean nearest-neighbor distance λ/σ vs. packing fraction ϕ for hard spheres. Thin solid line is theoretical prediction. Open circles are simulation data. Thin dashed line, thick dashed line, and solid lines are upper bounds.

neous media [10]. The latter work can be used to understand the critical issues involved when examining a digitized image of an actual material sample.

IV. MICROSTRUCTURE CHARACTERIZATION

Some of the different types of statistical correlation functions that have arisen in rigorous bounds on transport properties were described in the previous section. Until recently, application of such bounds (although in existence for almost thirty years in some cases) was virtually nonexistent because of the difficulty involved in ascertaining the correlation functions.

A. Unified Theoretical Approach

For statistically inhomogeneous systems of N identical d-dimensional spheres, Torquato [11] has introduced the general n-point distribution function $H_n(\mathbf{x}^m; \mathbf{x}^{p-m}; \mathbf{r}^q)$ and found a series representation of H_n which enables one to compute it. From the general quantity H_n one can obtain all of the aforementioned correlation functions and their generalizations [11]. This formalism has been generalized to treat polydispersed spheres, anisotropic media (e.g., aligned ellipsoids and cylinders), and cell models [3,6].

We have developed analytical expressions for the *chord-length distribution function* for models of porous media with a *polydispersivity in size* [12,13]. A new *coarse-graining* procedure has been obtained to generate and analyze a wide class of model microstructures [14].

The nearest-neighbor distribution function $H(r)$ is a fundamental quantity that statistically characterizes a random system of particles (including liquid structure). We have found analytical expressions for $H(r)$ for nontrivial particulate models up to the *random*

close-packing density [15].

Using $H(r)$ we have been able to obtain new and fundamental rigorous results for the *mean nearest-neighbor distance* λ between particles [16]. In particular, we have found an excellent approximation to λ for equilibrium hard spheres that is valid up to random close packing and rigorous upper bounds on λ. We have proven that a certain region in the ϕ-λ plane is prohibited to ergodic, isotropic hard spheres. (shaded region in Fig. 2).

We have very recently developed an exact algorithm to compute $H(r)$ and other void statistics [17]. Moreover, we have extracted various statistical measures from digitized representations of consolidated-sphere models [18].

The important topological property of connectedness is reflected in the two-point *cluster function* which we have evaluated exactly for a certain contimuum percolation model [19].

B. 3D Imaging Using X-Ray Tomography

We have very recently obtained high-resolution $3D$ digitized representation of a Fountainbleu sandstone using x-ray tomographic techniques [20]. This digitized representation is used to extract a number of morphological characteristics of the sample. Figure 3 shows a slice of the sandstone which has a porosity of 0.15. Figure 4 depicts the two-point probability function obtained from all of the slices.

V. CROSS-PROPERTY RELATIONS

An intriguing fundamental as well as practical question in the study of heterogeneous materials is the following: Can different properties of the medium be *rigorously* linked to one another? Such cross-property relations become especially useful if one property is more easily measured than another property. For example, it is difficult to measure the permeability k in situ.

Torquato [21] derived the first rigorous relation connecting the permeability k to the mean survival time τ of a porous medium:

$$k \leq D\phi_1\tau \,. \tag{6}$$

Generally, inequality (6) is not sharp because τ is a reflection of the entire pore space, whereas k is a reflection of the *dynamically connected* part of the pore space.

More recently, Avellaneda and Torquato [22] derived the first rigorous *equality* connecting the permeability to the *effective electrical conductivity* of a porous medium *containing a conducting fluid of conductivity* σ_1 *and an insulating solid phase*:

$$k = \frac{L^2}{8F} \,, \tag{7}$$

where $F = \sigma_1/\sigma_e$ is the *formation factor* and L is a length parameter which is a weighted sum over the viscous relaxation times associated with the time-dependent Stokes equations.

It has been conjectured that for isotropic media possessing an arbitrary but connected pore space, the following relation holds [23]:

$$k \leq \frac{D\tau}{F} \,. \tag{8}$$

We have continued to seek and test cross-property relations that connect the fluid permeability of porous media with diffusion properties, such as diffusion relaxation times, obtainable from NMR experiments, and the *electrical conductivity* [24,25]. Based on the above rigorous results, it has been proposed [24] that the approximate relation

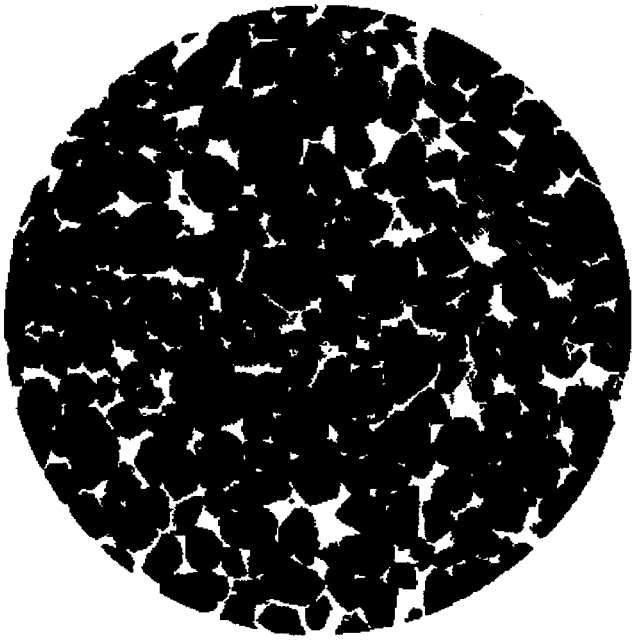

Figure 3: Sample filtered slice of Fountainbleu sandstone. The black region corresponds to the grain phase.

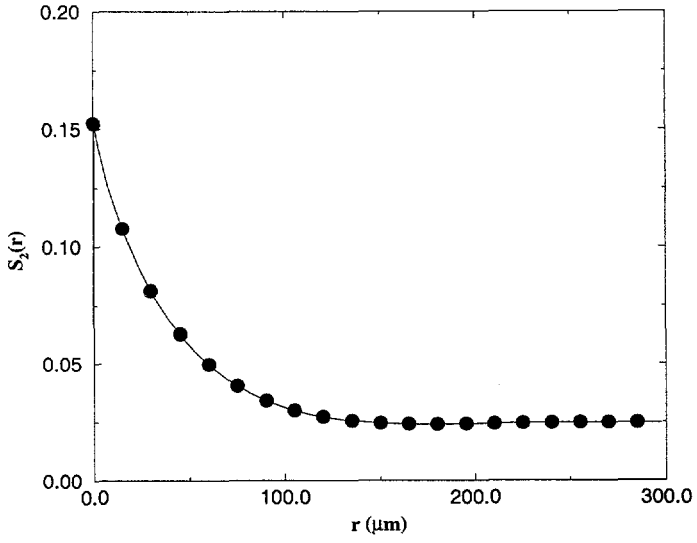

Figure 4: Two-point probability function vs. distance for Fountainbleu sandstone.

$$k \approx \phi_1 \frac{D\tau}{F} . \tag{9}$$

should be accurate for a large class of porous media.

To test cross-property relation (9), we have recently analyzed the 3D tomographic image of the aforementioned Fountainbleu sandstone (see Fig. 3) [20]. The quantity τD was determined to be 154 μm^2 from Brownian-motion simulations, F^{-1} was rigorously bounded from above by the value 0.089 using three-point information [7], and ϕ_1 was found to be 0.15. Thus, relation (9) predicts $k \approx 2.1 \mu m^2$, which is in relatively good agreement with the experimental value [25] of 1.3 μm^2.

The attentuation of elastic waves in fluid-saturated porous media depends on their effective elastic moduli. We have rigorously linked the conductivity to the elastic moduli of the medium [26-28].

ACKNOWLEDGMENTS

Support for this work was provided by the DOE under Grant DE-FG05-92ER14275.

REFERENCES

1. A. H. Thompson et. al., "Deuterium Magnetic Resonance and Permeability in Porous Media," *J. Appl. Phys.* **65**, 3259 (1989).
2. S. Torquato and M. Avellaneda, "Diffusion and Reaction in Heterogeneous Media," *J. Chem. Phys.* **95**, 6477 (1991).
3. S. Torquato, "Random Heterogeneous Media: Microstructure and Improved Bounds on Effective Properties," *Appl. Mech. Rev.* **44**, 37 (1991).
4. A. E. Scheidegger, *The Physics of Flow through Porous Media* (University of Toronto Press, Toronto, 1974).
5. J. Rubinstein and S. Torquato, "Flow in Random Porous Media: Mathematical Formulation, Variational Principles, and Rigorous Bounds," *J. Fluid Mech.* **206**, 25 (1989).
6. S. Torquato, "Unified Methodology to Quantify the Morphology and Properties of Inhomogeneous Media," *Physica A*, 79 (1994).
7. L. V. Gibiansky and S. Torquato, "Geometrical Parameter Bounds on Effective Properties of Composites," *J. Mech. Phys. Solids*, in press.
8. N. Martys, S. Torquato, and D. P. Bentz, "Universal Scaling of Fluid Permeability for Sphere Packings," *Physical Review E*, **50**, 403 (1994).
9. I. C. Kim and S. Torquato, "Effective Conductivity of Composites Containing Spheroids: Simulations and Comparison to Theory," *Journal of Applied Physics*, **74**, 1844 (1993).
10. D. Coker and S. Torquato, "Simulation of Diffusion and Reaction in Digitized Heterogeneous Media," *Journal of Applied Physics*, **77** (1995).
11. S. Torquato, "Microstructure Characterization and Bulk Properties of Disordered Two-Phase Media," *J. Stat. Phys.* **45**, 843 (1986).
12. B. Lu and S. Torquato, "Chord-Length and Free-Path Distribution Functions in Many-Body Systems," *Journal of Chemical Physics* **98**, 6472 (1993).
13. S. Torquato and B. Lu, "Chord-Length Distribution Function for Two-Phase Random Media," *Physical Review E*, **47**, 2950 (1993).
14. R. Blumenfeld and S. Torquato, "A Coarse-Graining Procedure to Generate and Analyze Heterogeneous Materials: Theory," *Physical Review E*, **48**, 4492 (1993).

15. S. Torquato, "Nearest-Neighbor Statistics for Random Packings of Hard Spheres and Disks," *Physical Review E*, **51**, 3170 (1995).
16. S. Torquato, "Mean Nearest-Neighbor Distance in Random Packings of D-Dimensional Hard Spheres," *Physical Review Letters*, **74**, 2156 (1995).
17. M. D. Rintoul and S. Torquato, "An Exact Algorithm to Compute Void Statistics for Random Arrays of Disks," submitted to *Physical Review E.*
18. D. Coker and S. Torquato, "Extraction of Morphological Quantities from a Digitized Image," *Journal of Applied Physics*, **77** (1995).
19. E. Cinlar and S. Torquato, "Exact Determination of the Two-Point Cluster Function for One-Dimensional Continuum Percolation," *Journal of Statistical Physics*, **78**, 827 (1995).
20. D. Coker, S. Torquato, and J. Dunsmuir "Morphological and Physical Properties of Fountainebleu Sandstone from Tomographic Analysis," to be submitted to *Journal of Applied Physics*
21. S. Torquato, "Relationship Between Permeability and Diffusion-Controlled Trapping Constant of Porous Media," *Phys. Rev. Lett.* **64**, 2644 (1990).
22. M. Avellaneda and S. Torquato, "Rigorous Link Between Fluid Permeability, Electrical Conductivity, and Relaxation Times for Transport in Porous Media," *Phys. Fluids A* **3**, 2529 (1991).
23. S. Torquato and I. C. Kim, "Cross-Property Relations for Momentum and Diffusional Transport in Porous Media," *Journal of Applied Physics*, **72**, 2612 (1992).
24. L. M. Schwartz, N. Martys, D. P. Bentz, E. J. Garboczi, and S. Torquato, "Cross-Property Relations and Permeability Estimation in Model Porous Media," *Physical Review E*, **48**, 4584 (1993).
25. L. M. Schwartz, F. Auzerais, J. Dunsmuir, N. Martys, and S. Torquato, "Transport and Diffusion in Three Dimensional Composite Media," *Physica A*, **207**, 28 (1994).
26. L. V. Gibiansky and S. Torquato, "Link Between the Conductivity and Elastic Moduli of Composite Materials," *Physical Review Letters*, **18**, 2927 (1993).
27. L. V. Gibiansky and S. Torquato, "Rigorous Link Between the Conductivity and Elastic Moduli of Fiber-Reinforced Composite Materials," *Philosophical Transactions of the Royal Society*, in press.
28. L. V. Gibiansky and S. Torquato, "Connection Between the Conductivity and Elastic Moduli of Isotropic Composite Materials," *Proceedings of the Royal Society of London A*, in press.

NMR STUDIES OF MULTIPHASE FLOWS. II

S. A. Altobelli, A. Caprihan, E. Fukushima, I. J. Lowe, and L. Z. Wang

The Lovelace Institutes
2425 Ridgecrest Dr., SE, Albuquerque, NM 87108 USA

ABSTRACT

NMR techniques for measurements of spatial distribution of material phase, velocity and velocity fluctuation are being developed and refined. Versions of these techniques which provide time average liquid fraction and fluid phase velocity have been applied to several concentrated suspension systems which will not be discussed extensively here. Technical developments required to further extend the use of NMR to the multi-phase flow arena and to provide measurements of previously unobtainable parameters are the focus of this report.

INTRODUCTION AND HISTORY

Nuclear magnetic resonance (NMR) has been used to study flowing fluids at The Lovelace Institutes (TLI) for the past ten years. The advantage of the NMR method for flow measurements is many-fold. Among the more obvious are that it is non-invasive and that, for certain materials, it can examine a flow system without any opaqueness problems. Among the possibly less obvious advantages is that the technique can measure many flow parameters not limited simply to velocity and concentration but also to diffusion, turbulence, acceleration, etc., as primary parameters (as opposed to secondary parameters that are derived from the primary parameters). The advent of NMR imaging (NMRI) allows us to spatially resolve all such parameters.

We have embarked on a program to study various properties of multiphase flows by NMR. In particular, we wish to develop new techniques and apply them to problems in various fields. The initial objective, five years ago under BES funding, of showing that spatially resolved measurements of velocity and concentration of liquid/solid multiphase flows was possible at any concentration of the solid component, has been fulfilled and some results were presented at the Tenth Symposium on Energy Engineering Sciences in 1992 [1]. Our current objectives are, on the one hand, to extend such measurements to higher order parameters such as diffusion and fluctuations of velocity and, on the other hand, to improve the NMR hardware to permit faster data acquisition which will yield better data for such parameters. In flows of concentrated suspensions and granular materials velocity fluctuations are hypothesized to be a crucial element of multi-phase transport processes [2, 3]. In this report, we describe progress made in several of these areas which represent pre-conditions to actually making such measurements in multiphase flows.

NMR AND LDA VELOCIMETRY IN A CURVED DUCT

In theory, NMR velocity measurements can produce 2- and 3-d datasets and arbitrary velocity components can be measured. In practice, mainly simple flows have been used to validate NMR methods, and the accuracy and precision of NMR velocity measurement techniques in complicated flows have not been assessed. An NMR velocity measurement system based on first order phase methods, and appropriate for measurement of a complex flow field with a primary velocity component and two smaller "secondary" components was implemented. Velocity dependent mis-registration was minimized by placing the phase-encoding interval immediately before the read-out interval and using a short echo-time. A geometry amenable to reliable measurement with transmission mode laser Doppler anemometry was chosen. The LDA measurements were done at the University of New Mexico in the laboratory of Prof. R. Truman.

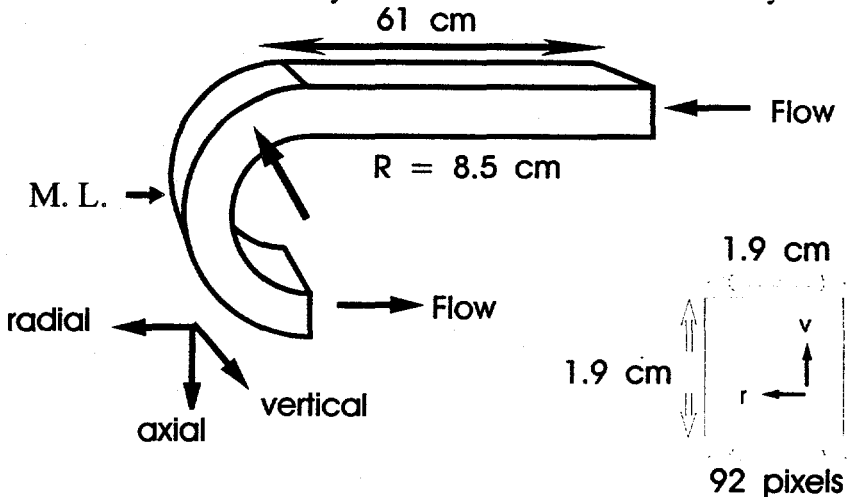

Figure 1. The dimensions of the Plexiglas flow phantom are shown. Flowing water entered a 61 cm straight duct, and turned in a section with centerline radius of 8.5 cm. Velocity components were measured after 90 ° of bend (M.L.). The cross section of the duct was 1.9 cm on a side.

A duct having square cross-section (1.9 ± 0.05 cm on a side) was constructed from Plexiglas sheet and cylinder stock. The dimensions of the duct are shown in Figure 1. Water from a constant height reservoir flowed through flexible tubing into a 61 cm straight section of square duct, turned through a 180° section of duct, with centerline radius 8.5 cm, and exited through a circular orifice into a second flexible tube. Tap water was used in the laser Doppler measurements. Water doped with Gd ($T_1 \approx 0.25$ s) was used in the NMR measurements.

The rf coil was modified to allow insertion of the phantom in the configuration shown. Slots were cut in the outer can and between the "rungs" in the resonant circuit. To install the flow model, the coil was partially disassembled, the curved section inserted through the rungs, the efflux tube connected, and the rf coil reassembled. The fact that the downstream end of the curved section was interrupted was less than optimal from the standpoint of comparison with previous results.

Three orthogonal components of velocity in a curved duct of square cross-section were measured with NMR, and two velocity components were also measured with laser Doppler techniques. Comparison between the two methods showed that accurate measurements of 3-dimensional flows can be made with NMR phase methods. Experiments using static references gave the most reliable measurements in low velocity regions. In Figure 2, a set of low flow rate measurements are shown.

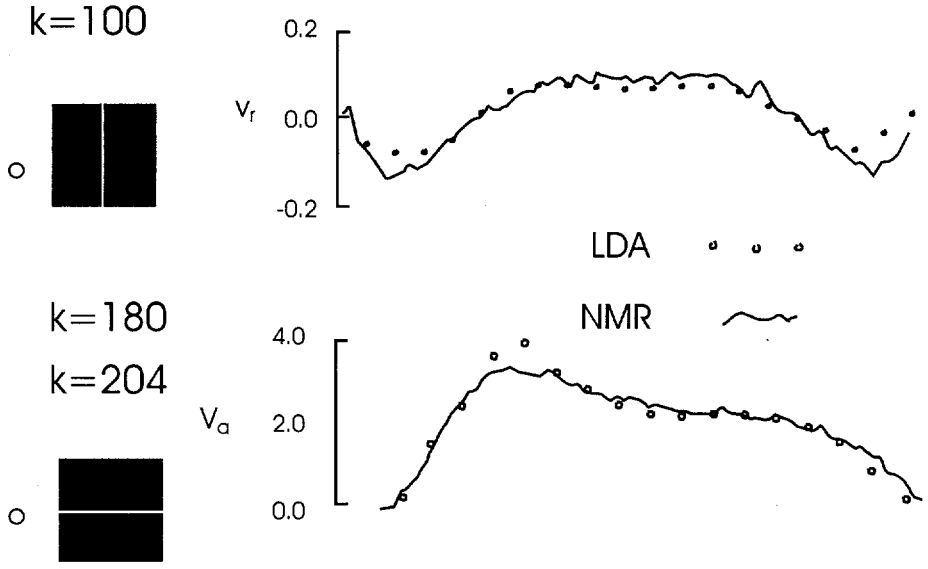

Figure 2. Comparisons between NMR (continuous lines) and LDA (points) are shown for the two velocity components measured with LDA. The schematics on the left show the locations of the measurement traverses, "O" refers to the outside of the curved tube.

At low flow rates, a single pair of vortices similar to low Dean number flow in a curved tube, symmetric about the plane containing the duct axis, is observed. The sense of the secondary flow is also the same as in a curved tube -- outward along the axis of symmetry, and inward along the walls. NMR velocimetry provides measurements over the cross-section, as opposed to measurements along a single line, and an example obtained at a higher flow rate is given in Figure 3. A vector plot shows the distribution of the secondary velocity components in the duct.

Below the vector plot, images of the velocity components are shown. The outer curved wall is shown on the left of the images and the vector plot. At this flow, two vortex pairs are prominent. The LDA confirmed the qualitative differences observed with NMR as a function of flow rate.

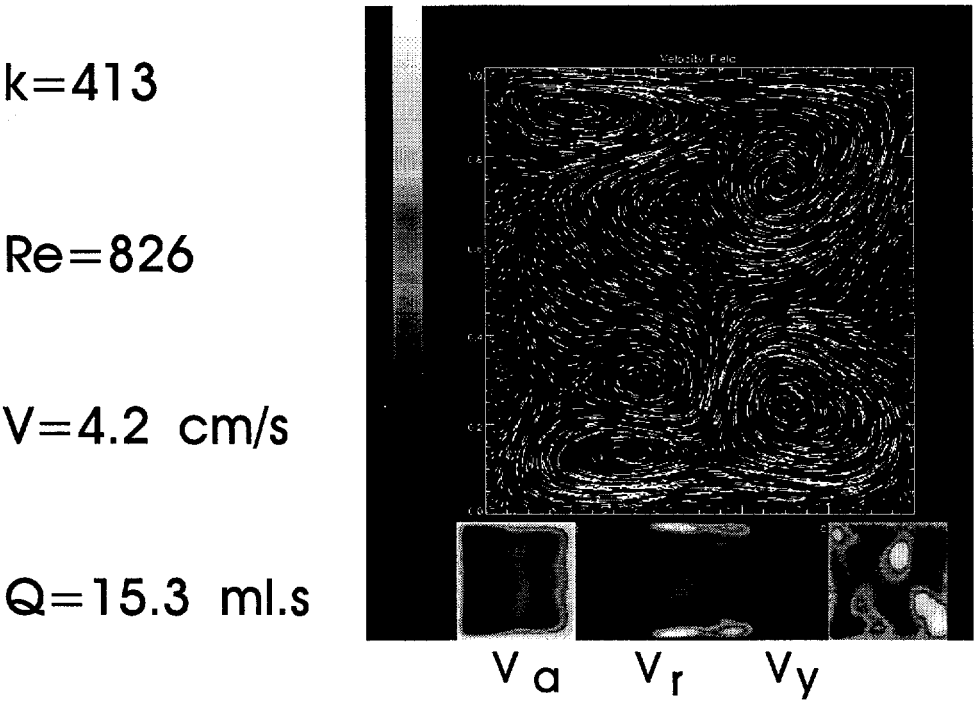

Figure 3. NMR data obtained in the curved duct at a flow of 15.3 cm^3/s are shown. a vector plot shows the presence of multiple pairs of vortices. The outer edge of the curved duct is on the left, as in Figures 1 and 2.

NMR DIFFUSION AND TURBULENCE MEASUREMENTS

Some of the techniques for measuring flow velocity by NMR were reviewed three years ago [1] and will not be reviewed here but the NMR methods for measuring molecular diffusion and turbulent diffusivity will be described.

Molecular diffusion measurements by NMR is an area we have gone into in the past two years. NMR can measure diffusion in the following way. In any NMR experiment, the nuclei with gyromagnetic ratio γ precess about the magnetic field B at frequency f according to the Larmor theorem: $f=(\gamma/2\pi)B$. Suppose an ensemble of spins is made phase coherent at $t=0$ and a magnetic field gradient g is applied for a time δ. The gradient causes spins at different locations z, to precess in a magnetic field intensity distributed according to gz, i.e., the spread of frequency across a distance z is $(\gamma/2\pi)gz$ and the incremental phase gain (or less) is $(\gamma/2\pi)gz\delta$. If, an equal but opposite gradient is applied at some later time Δ, the incremental phase changes reverse exactly and the ensemble finds itself with a regained coherence, leading to an unattenuated NMR signal. If, however, there is diffusion during the interval Δ, the full coherence will not be regained because the incremental phase changes during the two gradient pulses will not be equal

and opposite. Thus, NMR can be used to measure the diffusion coefficient by the signal attenuation caused by the diffusive motion of the molecules during an appropriately designed pulse sequence. In fact, any other incoherent motion will also attenuate the signal and this fact is used to study turbulent diffusivity.

Diffusion in restricted spaces can be studied by NMR, too, because the technique, as described above, measures the spin displacements in the interval Δ and the barriers to diffusion modifies the range of displacements. Because barriers can only limit the range of molecular motion, diffusion in restricted spaces can only increase the signal amplitude over unrestricted diffusion. There is an inherent difficulty that as more restrictive or, equivalently, more diffusive systems are studied, the gradient pulses that are used to define the range of incoherence will need to be made more effective. In the expression for the phase increment, given above, the only variables that can be changed for any given system are g and δ, the amplitude and duration of gradients. Because there is a practical limit to how large the gradient amplitude g can be made, there is a need to consider lengthening the duration δ. This is the root cause of much of our present research because much of the past derivations relating the diffusion coefficient D, the restricted spacing a, and the signal, depend on an assumption that the gradient pulse length δ obeys the relation $\delta << a^2/D$, i.e., it must be short enough that the molecule will not diffuse across the restricted region of dimension a during δ.

NARROW PULSE APPROXIMATION IN RESTRICTED DIFFUSION

An alternative manifestation of NMR signals being sensitive to molecular motion, besides the measurements of velocities, is the use of NMR to investigate molecular diffusion and the influence of barriers on such diffusion. Qualitatively, this is possible because any random molecular motion that takes place between two gradient pulses, one to dephase the spins and the other to rephase them, leads to an incomplete rephasing of the spins and shows up as a signal attenuation. Standard techniques for microstructure determination has existed for over three decades provided the magnetic field gradients used can be considered so short that no diffusion takes place during them.

The problem of diffusion in the presence of barriers, considered in this and next sections of this report, is an important one in many multiphase flow applications. The interphase boundaries usually represent significant barriers to diffusion so that any information on such boundaries leads to information about the multiphase structure.

Barriers to diffusion reduces the attenuation caused by diffusion because they reduce the range of translational motion for the spins. Therefore, ever stronger gradients must be used to study smaller and smaller restricted spaces. Because there is a limit to the strength of magnetic field gradients that can be created, there is a need to increase the duration of the gradient pulses. Thus, it is possible to violate the condition of "infinitely" narrow pulses, as diffusion is studied for smaller restricted regions. With the recent impetus for probing diffusion in ever smaller restricted spaces, this has become a meaningful question. A general expression for the attenuation has been derived from stochastic theory of random spin motion with an assumption of Gaussian displacements. The echo attenuation is divided into contributions A and B. A represents the contribution in the presence of the gradient while B is the contribution with the gradient off so that $F=A/(A+B)$ must be small for the narrow pulse approximation to hold.

Figure 4 is a plot of equal values of F as a function of two times, the duration of the gradient pulses δ, and the interval between the gradient pulses Δ, both in units of a^2/D which is the time for a molecule to diffuse with a diffusion coefficient D across the restricted space of dimension a.

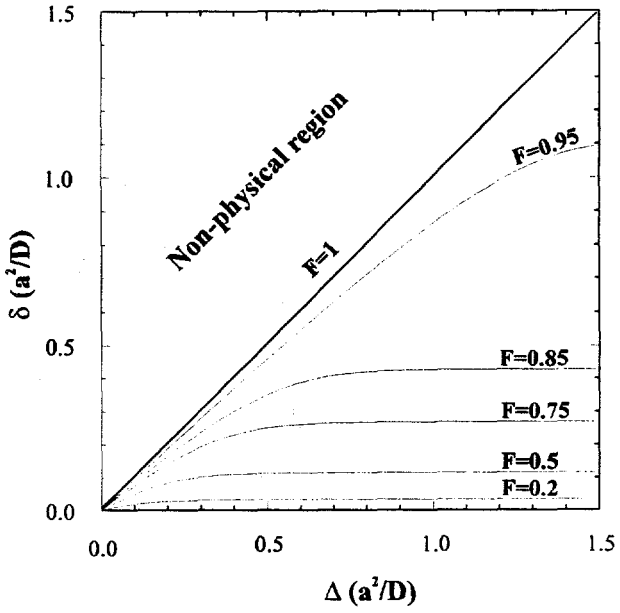

Figure 4. The fraction F of the total attenuation occurring during the application of the gradient pulses or a PGSE experiment as a function of the time intervals δ and Ω.

We have performed an alternative derivation of the same criterion for the validity of narrow pulse expressions for restricted diffusion from the diffraction-like behavior of NMR signal attenuation as a function of $qa=\gamma g\delta a/2\pi$, where q is, in effect, a reciprocal lattice vector for restricted diffusion [4]. In the narrow pulse approximation, the signal has minima at multiples of $q=1/a$. From the results of Blees [5], we plotted contour lines of constant fractional deviation of a particular minimum as a function of $\delta D/a^2$ and $\Delta D/a^2$ as before and the curves have shapes identical to those of Fig. 2.

We have found that the condition $F<<0.1$ is equivalent to a 5% shift in the second minimum position in qa. Although neither of these conditions seems very strict, they lead to the conclusion that gradient pulse duration δ must be much shorter than $0.02D/a^2$ in order for the narrow pulse expressions to be valid, a surprisingly strong criterion.

ANALYTICAL EXPRESSION FOR TIME-VARYING GRADIENTS

Although analytic expressions for NMR echo signals from an assembly of atomic nuclei undergoing diffusion in free and confined spaces were derived more than 30 years ago, a general expression without the assumption that molecular diffusion does not take place during the gradient pulses still does not exist. This is a problem that is gaining in importance as more and more smaller spaces or larger diffusion coefficients are studied. That this is so can be seen by the fact that the appropriate time unit for these problems is a^2/D which is how long a molecule with

diffusion coefficient D takes to diffuse across a restricted space a. Thus, smaller restricted spaces has the same effect as larger D.

We have derived an approximate analytical solution for diffusion in the presence of a gradient pulse that is not infinitesimally short by approximating the pulse with a series of gradient impulses each of which has a known narrow-pulse solution. We examined the convergence of the solution as a function of the order of the approximation, i.e., the number of impulses used, and found that 8 impulses is sufficient for most combinations of parameters. Because the method is general, it can be used for any shape gradient pulse, and its use is not limited only to rectangular pulses. Furthermore, the formalism is also applicable to non-uniform initial magnetization distribution.

STUDIES OF DIFFUSIVE AND TURBULENT SPECTRA

There have been suggestions of using gradient pulses that are tailored to probe particular frequency components of spectral density associated with coherent or incoherent motion [4]. We have derived relations for the signal attenuation as a function of sine and cosine coefficients of sinusoidal magnetic field gradients used during an otherwise standard NMR pulsed gradient spin echo diffusion experiments. We then performed experiments in three model systems: 1) diffusion measurements of water in an effectively unconfined space; 2) measurements of water diffusing between mica sheets spaced 25 μm apart; and 3) measurements turbulent diffusivity of water flowing in a circular pipe.

For water at room temperature in an unconfined space, the spectral density for diffusion is independent of frequency in the range studied, up to 100 Hz, as expected. On the other hand, in restricted spaces, deviation from the unconfined behavior is expected at the lower frequencies where the molecules have enough time to encounter walls. Experimentally, we measure the expected behavior, i.e., the spectral density is flat above 22 Hz but decreases below this threshold which is consistent with the known spacing between the mica sheets of 25 μm, as shown in Fig. 5.

We wish to extend this technique to the measurement of turbulent diffusivity. A preliminary experiment in water flowing in a circular pipe with Reynolds numbers between 2,000 and 12,000, yielded spectral densities that did not follow the correlation time-based curves used to fit spectral density for diffusion. This is to be expected because in turbulent diffusivity, the eddies are not uncorrelated as smaller ones are subdivided from the larger ones in order that the energy can be dissipated.

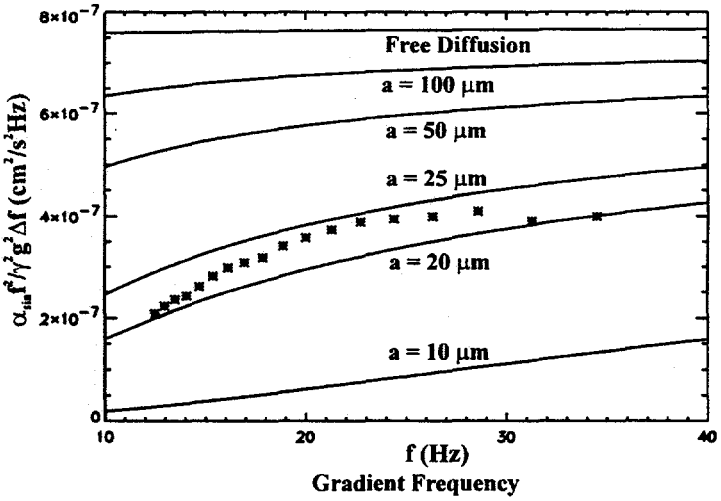

Figure 5. Results from spectral density of diffusion measurements (points) in a stack with 25 μm spacing shows good agreement with theoretical prediction. The technique is being evaluated for measurement of the size spectrum of turbulent eddies.

ACKNOWLEDGMENTS

This work was supported, in part, by the U. S. Department of Energy (DOE), Office of Basic Energy Sciences, via contract DE-FG03-93ER14316. Such support does not constitute an endorsement by DOE of the views expressed in this article. We benefited greatly from collaborations with R. C. Givler and L. A. Mondy of Sandia National Laboratories and A. L. Graham of Los Alamos National Laboratory in matters of multiphase flows.

1. S. A. Altobelli, A. Caprihan, E. Fukushima, and E.-K. Jeong, "Recent Results: NMR of Multiphase Flows," in Proceedings of the Tenth Symposium on Energy Engineering Sciences, May 11-13, 1992, Argonne National Laboratory, CONF-9205147; pp. 68-75.
2. J. T. Jenkins and D. F. McTigue, "Transport Processes in Concentrated Suspensions: The Role of Particle Fluctuations", In *Two Phase Flows and Waves* (D. D. Joseph and D. G. Schaeffer, eds.), Springer, 1990.
3 P. R. Nott and J. F. Brady, "Pressure-driven flow of suspensions: Simulation and Theory", *JFM* 1994, **275**, 157-199.
4. P. T. Callaghan, " Principles of Nuclear Magnetic Resonance Microscopy," Ch. 6-8, Oxford Univ. Press, New York, 1991.
5. M. H. Blees, J. Magn. Reson. A 109, 203 (1994).

INITIATION OF SLUG FLOW

Thomas J. Hanratty and Bennett D. Woods

University of Illinois
Urbana, Illinois 61801, U.S.A.

ABSTRACT

The initiation of slug flow in a horizontal pipe can be predicted either by considering the stability of a slug or by considering the stability of a stratified flow. Measurements of the shedding rate of slugs are used to define necessary conditions for the existence of a slug. Recent results show that slugs develop from an unstable stratified flow through the evolution of small wavelength waves into large wavelength waves that have the possibility of growing to form a slug. The mechanism appears to be quite different for fluids with viscosities close to water than for fluids with large viscosities (20 centipoise).

INTRODUCTION

The prediction of flow regimes is a central problem in the analysis of gas-liquid flows in pipes. Early work had used two-dimensional flow maps that employed variables such as the superficial gas and liquid velocities. These have proven unsatisfactory since they cannot represent the influence of the large number of variables that define multiphase systems. Pioneering works in this area are the papers presented by Dukler and his coworkers [1][2]. These papers suggest physical criteria and equations that define transitions from one regime to another. Flow maps can then be constructed for particular situations.

During the past 15 years the mechanisms suggested in references [1] and [2] have been examined more carefully and we now realize that some of the physics is flawed. This accounts for the failure of this approach to explain many observed phenomena. There is a need to develop an updated equation-based approach which utilizes improvements in our understanding of this problem.

This paper presents recent results on the transition from a stratified flow to a slug flow

in a horizontal pipe. Taitel & Dukler [1] suggest, on the basis of geometric arguments, that the height of the liquid in the stratified flow, h_L, needs to be larger than one-half of the pipe diameter, D, in order for a slug to form. This constitutes a necessary condition for the existence of slugs. A closer examination of data reveals that the proposed critical h_L/D is too large.

This paper summarizes results of a M.S. thesis from this laboratory [3] which relates the stability of slugs to the height of the liquid. The idea behind the analysis is quite simple: Slugs pick up liquid at the front as they propagate downstream and shed liquid at the rear. If the pickup rate is smaller than the shedding rate, slugs will decay. The critical problem is to define the volumetric shedding rate, Q_L.

Ruder et al [4] developed this idea by assuming the back of the tail as a Benjamin bubble so that

$$Q_L = A\left[0.542\ (gD)^{0.5}\right] \tag{1}$$

where A is the pipe area and D is the pipe diameter. This assumption provides only a limiting value of the critical h_L/D at small gas velocities. A series of studies were, therefore, carried out in which Q_L was measured for individual slugs. The system was air and water flowing in a horizontal pipe. The results of this study provide a necessary condition for the existence of a stable slug that is consistent with measurements.

For large h_L/D, Wallis and Dobson [5] suggested that the initiation of slugs might be considered to result from the stability of a stratified flow to long wavelength disturbances. The following critical condition was suggested:

$$U-u = K\left[\frac{g\rho_L H_G}{\rho_G}\right]^{\frac{1}{2}} \tag{2}$$

where U is the gas velocity, u, the liquid velocity and H_G, the height of the gas space. The use of an inviscid analysis gives K=1, but Wallis found for air and water that $K\approx\frac{1}{2}$. Taitel and Dukler adapted (2) to the geometry of a circular pipe and suggested that

$$K = \left(1-\frac{h_L}{D}\right) \tag{3}$$

The inviscid analysis yields a wave velocity, C, equal to u. Therefore, the inertia of the liquid is neither stabilizing nor destabilizing. Lin & Hanratty [6] carried out a viscous long wavelength analysis. The wave velocity is, then, not equal to u and liquid inertia is destabilizing. They found that K is a function of liquid viscosity. For water $K\approx\frac{1}{2}$; for liquids with viscosities greater than 20 centipoise, K=1.

Equation (2) has two important features. It suggests that a slug evolves directly from

a long wavelength disturbance that grows until it reaches the top of the pipe. It also suggests that the gas velocity needed to generate a slug increases with $D^{1/2}$. Measurements with air and water agree with this analysis [7]. However, studies with viscous liquids [8] reveal no influence of pipe diameter if the liquid viscosity is 20 centipoise or greater.

This disagreement suggests that the physical mechanism suggested by (2) is incorrect even though it correctly predicts the transition for an air-water flow. This paper summarizes recent results which show that slugs evolve from small wavelength waves and not from the direct growth of a large wavelength instability.

The implications of these new results from the viewpoint of predicting flow regimes is discussed.

STABILITY OF A SLUG

If conservation of mass is used in a frame of reference moving with a slug, the following equation is obtained for incompressible fluids:

$$\left(C-u_{LI}\right) A_{LI} - Q_L = A\left(1-\alpha\right)\frac{dL}{dt}, \tag{4}$$

where C is the slug velocity, u_{L1} the velocity of the liquid in the layer in front of the slug, A_{LI}, the area occupied by the liquid in front of the slug, α, the void fraction in the slug, L, the length of the slug and t, time. For a neutrally stable slug, dL/dt=0, and

$$A_{LI}^{C} = \frac{Q_L}{C-u_{LI}} \tag{5}$$

For $A_{L1}<A_{L1}^{C}$ slugs will decay; for $A_{L1}>A_{L1}^{C}$ slugs will grow.

If the back of a slug can be modelled as the nose of a bubble an equation for C similar to what is used for elongated bubbles in vertical tubes can be explored:

$$C=C_{\infty} + C_o u_{L3}, \tag{6}$$

where C_{∞} is the bubble velocity in a stationary fluid and u_{L3} is the average liquid velocity

$$u_{L3}=\frac{U_{SG} + U_{SL}}{1-(S-1)\alpha} \tag{7}$$

where U_{SG} is the superficial gas velocity, U_{SL}, the superficial liquid velocity and S the ratio of the gas and liquid velocities in the slug.

The second term in (7) represents the contribution of fluid convection to the slug velocity. For vertical flow with a turbulent liquid C_o has a value approximately equal to the ratio of the centerline and average velocities, $C_o \approx 1.2$.

The motion of the bubble relative to the liquid causes a displacement of liquid inside the slug given by

$$Q_L = \left(C - u_{L3}\right) A\left(1-\alpha\right) \tag{8}$$

Now if (6) is substituted into (8) and (5) the following relations are obtained:

$$Q_L = \left[C_\infty + \left(C_o - 1\right) u_{L3}\right] A\left(1-\alpha\right) \tag{9}$$

$$A_{LI}^{C} = \frac{\left[C_\infty + \left(C_o - 1\right) u_{L3}\right] 1-\alpha}{\left[C_\infty + C_o u_{L3} - u_{LI}\right]} \tag{10}$$

At large gas velocities u_{L1} can be neglected and $C_\infty << C_o u_{L3}$ so

$$A_{LI}^{C} = \frac{\left(C_o - 1\right)\left(1-\alpha\right)}{\left(C_o\right)} \tag{11}$$

If C_o=1.3 and $(1-\alpha) \approx 0.3$, equation (11) gives

$$\frac{A_{LI}}{A} = 0.16 \tag{12}$$

$$\frac{h_{LI}}{D} = 0.21 \tag{13}$$

DESCRIPTION OF EXPERIMENTS

The flow facility consists of a horizontal pipeline with a diameter of 0.0953 m and a length of 26.5 m. The experiments were conducted at atmospheric conditions. The gas and liquid phases were combined at the beginning of the pipeline in a tee section with the liquid phase flowing in the run and the gas phase entering from the top of the tee.

Measurements of the variation of the liquid holdup were obtained with a conductance probe that consists of two parallel chromel wires. A complete description of the film height analyzer, including a circuit diagram, may be found in Williams [9].

Conductance probes were used at $\frac{L}{D}$ = 200, 220, and 250. Two conductance probes are needed to measure the slug velocity and the flow of liquid out the tail of the slug. A third conductance probe is added in order to observe changes in a slug as it progresses along the pipeline. The third probe also provides better measurements of C and Q_L by averaging results from the first and second probes and from the second and third probes.

Pressure pulsations associated with the passage of a slug were measured with a piezoresistive pressure transducer located 0.127 m downstream of the first conductance probe.

The transducer was mounted flush with the wall so that no disturbances were introduced into the flow.

The magnitude of the signals from the conductance probes give the liquid holdup, $(1-\alpha)$, when a slug passes and the height of the liquid layer when a stratified flow was present. The slug velocity, C, was determined from the time needed for a slug to move between two of the measuring stations.

Values of Q_L were obtained from measurements at two stations using the equation

$$Q_L = \left(C - u_{Ll}\right) A_{Ll} - \frac{dV}{dt} \tag{14}$$

This was accomplished by attaching a control volume fixed to back of the slug.

Term dV/dt was determined by measuring the change of the volume of the liquid inside the control volume between two stations. The front of the control volume was located sufficiently ahead of the slug so that the area of the stratified flow in the front of the slug, A_{Ll}, was the same at all three stations. Velocity u_{Ll} was calculated from A_{Ll} and the gas velocity by using stratified flow relations developed by Andritsos and Hanratty [10].

STABILITY OF SLUGS

Measurements of Q_L are presented in Figure 1. It is noted that they agree with the Benjamin solution only for small values of U_{SG}. These measurements and equation (5) were used to calculate critical values of A_{Ll} (or h_{Ll}/D). A trace obtained from the conductance probes is shown in Figure 2. Peaks could be identified as slugs from measurements of pressure pulses. Neutral stability is designated by the line indicating the stability height. The correlation is not perfect, but there is a tendency to find growing slugs when $A_{Ll} > A_{Ll}^{C}$ and decaying slugs when $A_{Ll} < A_{Ll}^{C}$.

Values of the critical h_{Ll}/D for different U_{SG}, calculated from (5) are shown as the dashed curve in Figure 3. The solid curve is the stability condition for a stratified flow. The points are the observed h_L/D at which slugs appear for a fixed gas flow. At low gas velocities the necessary condition for the existence of slugs lies below the stability condition for a stratified flow. However, at high gas velocities the opposite is the case. Good agreement is noted between the observed transition at large U_{SG} and the necessary condition for the existence of a slug.

The curve representing the stability of a stratified flow would be shifted to the left with increasing gas density. Therefore, at sufficiently high gas densities one could expect that the initiation of slugging would be defined by stability conditions for a slug at all gas flows, rather than just at high gas flows.

The asymptotic behavior of the dashed curve in Figure 3 gives a critical $h_L/D \approx 0.21$. This is exactly the prediction from (11) if $C_o = 1.31$. Measurements of slug velocity are represented quite well by the equation

$$C = \left\{ \left[0.541 (gD)^{\frac{1}{2}} \right]^2 + \left[1.31 \left(U_{SG} + U_{SL} \right) \right]^2 \right\}^{\frac{1}{2}} \tag{15}$$

From (7) and (15) it is observed that

$$\frac{C_o}{1 + (S-1)\alpha} = 1.31 \tag{16}$$

Therefore C_o=1.31 corresponds to a slip ratio of 1.

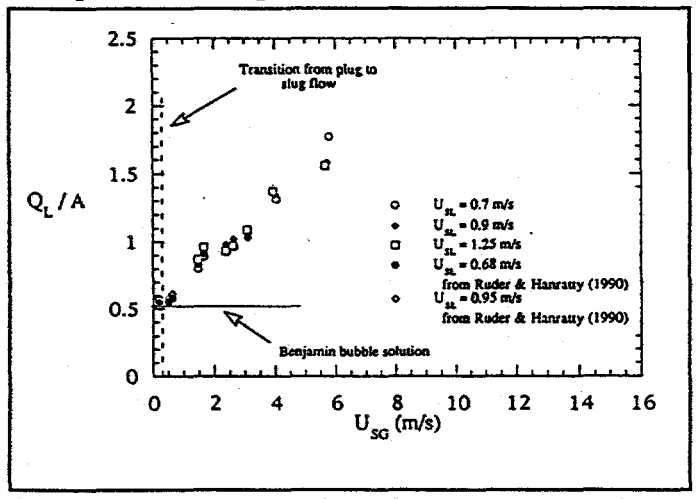

Figure 1 The mean value of the shedding velocity Q_L/A at each experimental flow condition as a function of the local superficial gas velocity.

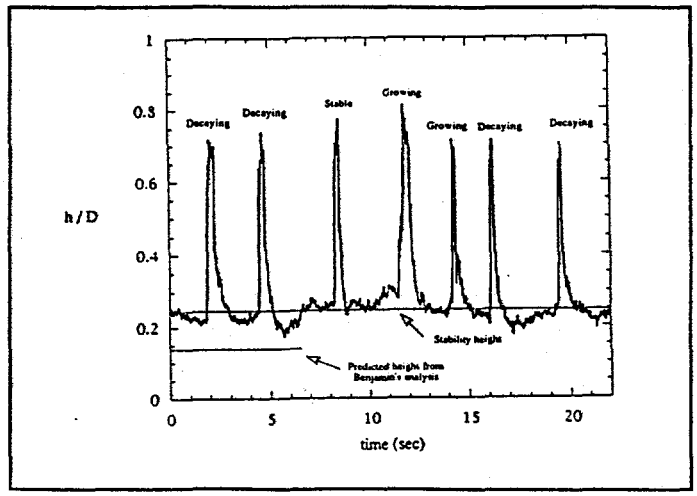

Figure 2 Liquid holdup profile at L/D=250 for U_{SG}=4.35 m/s and U_{SL} = 0.7 m/s.

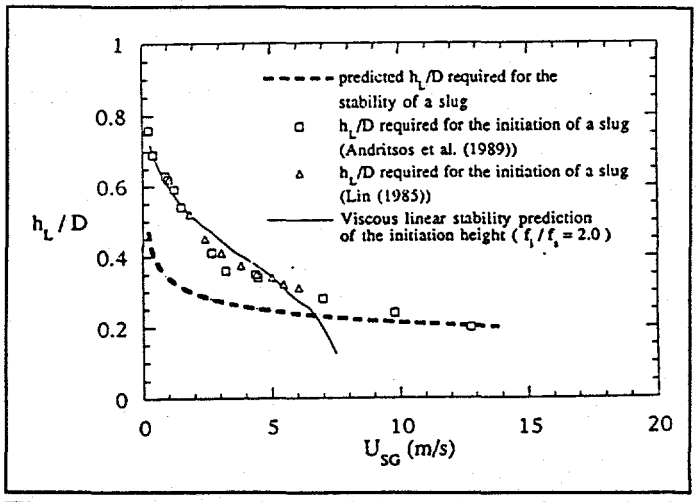

Figure 3 Comparison of the height of the liquid layer required for a stable slug with observations of the height of the liquid required to initiate a slug. (D=0.0953 m, Air - water system)

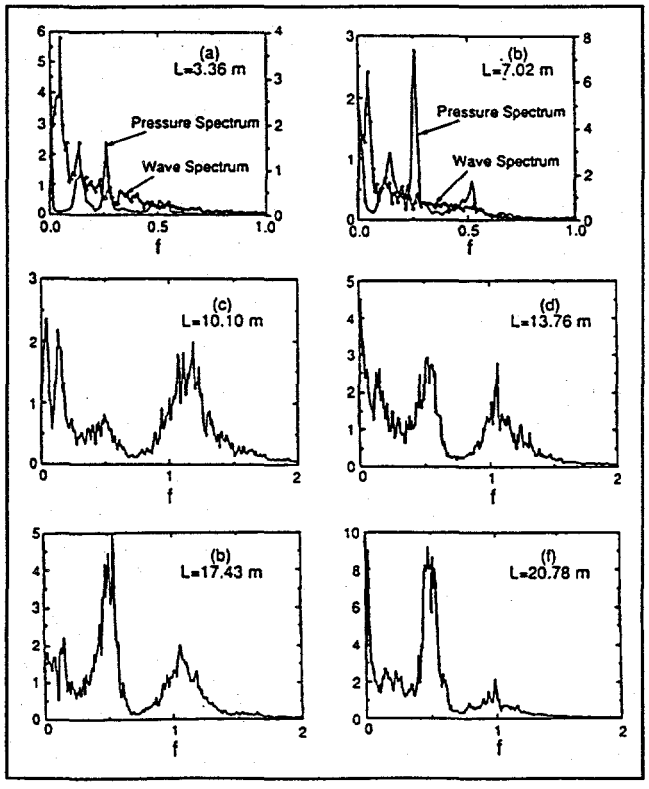

Figure 4. Power spectra of a liquid flow close to transition (u_{SG}=1.0m/s). The dimensionless spectra density functions are multiplied by 10^6. Wave spectra are on the left ordinate. Pressure spectra are on the right.

STABILITY OF A STRATIFIED FLOW

The transition to slug flow shown in Figure 3 for small gas velocities is governed by the stability of stratified flow. The mechanism for this transition for air/water has recently been explored by Fan et al [11]. A carefully designed entry was used to bring the gas and liquid together smoothly. Conductance probes were located along the pipeline to study the evolution of waves to form a slug.

Measured wave spectra are shown in Figure 4 for U_{SG}=1 m/s. The abscissa is the frequency (in cps) made dimensionless with $\sqrt{gD}$. The ordinate is the dimensionless spectral density function. The measurements at L=3.36 m and at L=7.02 m show a primary peak at f=0.06 (0.6 cps) and a secondary peak at f=0.12 (1.2 cps). These would correspond to very long wavelength waves that are observed visually as a swell. They would be predicted to appear by long wavelength theory. These waves do not evolve into a slug. Two peaks at f=0.12 and f=0.25 are observed in the spectral density function for the pressure fluctuations.

The peaks at f=0.06 and f=0.12 are still evident at L=10.1 m, but a peak with a large amount of energy appears at f=1.2 (12 cps). This corresponds to a capillary-gravity wave generated by Jeffrey's sheltering mechanism. A peak with a smaller amount of energy is also observed at f=0.5 (5 cps). As discussed in [11] the larger wavelength wave evolves from the f=1.2 wave through a resonance mechanism. This peak grows with distance downstream and the higher frequency peak shifts from f=1.2 to f=1.0. At 20.78 m, the f=0.5 wave is dominant. In a longer pipe this wave could stabilize to a fixed height (at which energy fed by the gas flow is balanced by viscous dissipation) or it could continue to grow until it breaks or forms a slug. There appears to be a critical liquid height (larger than that required for the existence of a stable slug), below which slugs cannot form from these waves.

The mechanism for the formation of slugs in these experiments at low gas flows appears to be different from what is suggested by (2). This is a paradox since equation (2) does a good job in predicting the initiation of slugs for liquids with viscosities close to that of water.

Figure 5 shows transition data obtained for a 100 cp liquid in a 9.53 cm pipe. The open triangular points represent a transition to slugs. The open squares indicate a transition to large amplitude waves. Because of the large viscosity, waves of the type described in Figure 4 are not present. The stratified flow that exists to left of the triangles has a smooth interface.

The transition points at large U_{SG} are, more than likely, defined by the stability condition for a slug, equation (5). However, it is noted by comparing Figures 3 and 5 that transition occurs at slightly higher h_L/D for the more viscous liquid. This suggests that C_o in (6) could be larger for large viscosity liquids, as has been found for large bubbles in a vertical tube.

At small gas flows the initiation of slugs, shown in Figure 5, occurs because of an instability of the stratified flow. A comparison of Figures 3 and 5 shows that larger values of h_L/D are required for an instability to occur with large viscosity liquids. The waves described in Figure 4 cannot occur. The first instability of the stratified flow occurs when the gas gap becomes small enough (for a given gas flow, U_{SG}) that the gas velocity above the liquid can cause a Kelvin-Helmholtz instability. The first disturbances that appear at the interface are capillary-gravity waves. These rapidly evolve into slugs by a mechanism which

has not been identified. The solid curve in Figure 5 represents the critical condition for the initiation of a Kelvin-Helmholtz instability.

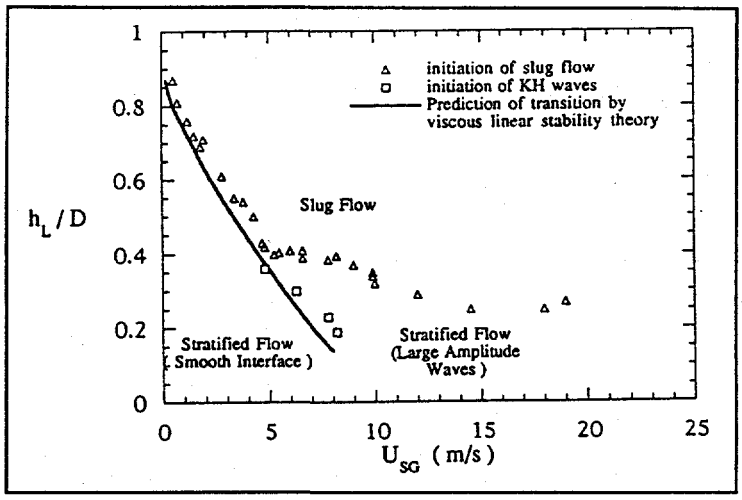

Figure 5 Initiation of slug flow or KH waves for a 100 cp liquid in a horizontal 9.53 cm pipe.

DISCUSSION

The flow regime criteria developed by Dukler and his coworkers have had an important impact on the analysis of two-phase flows. They are widely used - despite the recognition that they do not always give accurate results. Recently, more careful attention has been given to the physics defining the transitions. It is now possible to use these new insights to develop improved predictions of flow regimes.

A necessary condition for the existence of slugs of $h_L/D=0.5$ was suggested in [1] on the basis of geometric arguments. This paper develops an improved definition of this condition by considering the stability of slugs.

Equation (2) along with the long wavelength viscous analysis of Lin & Hanratty [6] does a good job in predicting the evolution of slugs from the instability of a stratified flow if the liquid viscosity is close to that of water. However, the observed mechanism appears to be different from what is suggested by (2). This issue needs to be resolved.

The waves which eventually evolve into slugs for stratified air-water flows are generated by a mechanism whereby energy fed to the waves by gas phase pressure variations in phase with the wave slope is larger than energy dissipated by viscous effects. As the viscosity of the liquid increases the critical gas velocity for the appearance of these waves also increases. For large enough liquid viscosities these waves are not present. In this case slugs evolve from capillary-gravity waves generated by a Kelvin-Helmholtz mechanism, whereby destabilization results from pressure variations 180° out of phase with the wave height. When the height of the liquid layer is too small to sustain a stable slug these Kelvin-Helmholtz waves evolve into large amplitude irregular waves. Under these conditions the initiation of slugging is governed by the stability condition for slugs.

REFERENCES

1. Y. TAITEL and A. E. DUKLER, "A Model for Predicting Flow Regime Transitions in Horizontal and near Horizontal Gas-Liquid Flow," *Int. J. Multiphase Flow* 13, 577 (1977).
2. Y. TAITEL, D. BARNEA and A. E. DUKLER, "Modeling Flow Pattern Transitions for Steady Upward Gas-Liquid Flow in Vertical Tubes," *A.I.Ch.E. Journal* 26, 345 (1980).
3. B. K. WOODS, "Shedding Rates of Slugs in Two Phase Horizontal Pipe Flow," Ph.D. thesis, Univ. of Illinois, Urbana (1995).
4. Z. RUDER, P. J. HANRATTY and T. J. HANRATTY, "Necessary Conditions for the Existence of Slugs," *Int. J. Multiphase Flow* 15, 135 (1989).
5. G. B. WALLIS and J. E. DOBSON, "The Onset of Slugging in Horizontal Stratified Air-Water Flow," *Int. J. Multiphase Flow* 1, 173 (1973).
6. P. Y. LIN and T. J. HANRATTY, "Prediction of the Initiation of Slugs with Linear Stability Theory," *Int. J. Multiphase Flow* 12, 79 (1986).
7. P. Y. LIN and T. J. HANRATTY, "Effect of Pipe Diameter on Flow Patterns for Air-Water Flow in Horizontal Pipes," *Int. J. Multiphase Flow*, 13, 13 (1987).
8. N. ANDRITSOS, L. WILLIAMS and T. J. HANRATTY, "Effect of Liquid Viscosity on the Stratified-Slug Transition in Horizontal Pipe Flow," *Int. J. Multiphase Flow*, 15, 877 (1989).
9. L. R. WILLIAMS, "Effect of Pipe Diameter on Horizontal Annular Two-Phase Flow," Ph.D. thesis, Univ. of Illinois, Urbana (1990).
10. N. ANDRITSOS and T. J. HANRATTY, "Influence of Interfacial Waves in Stratified Gas-Liquid Flows," *A.I.Ch.E. Journal* 33, 444 (1987).
11. L. FAN, F. LUSSEYRAN and T. J. HANRATTY, "Initiation of Slugs in Horizontal Gas-Liquid Flows," *A.I.Ch.E. Journal* 11, 1741 (1993).

THE DRIFT FORCE ON AN OBJECT IN AN INVISCID WEAKLY-VARYING ROTATIONAL FLOW

Graham B. Wallis

Thayer School of Engineering, Dartmouth College
Hanover, NH 03755 U.S.A.

ABSTRACT

The force on any stationary object in an inviscid incompressible extensive steady flow is derived in terms of the added mass tensor and gradient of velocity of the undisturbed fluid. Taylor's theorem is extended to flows with weak vorticity. There are possible applications to constitutive equations for two-phase flow.

INTRODUCTION

Any vector field (e.g., velocity) may be generated by a combination of flux and circulation sources. For example, an object in a potential flow may be "created" by putting a distribution of dipoles over its surface, to represent the jump in potential there, or a set of circulation source loops around its surface, to account for the jump in velocity [1]. A set of internal sources and sinks could also be used. Though various combinations of these elements can be selected, the resulting system has a unique dipole moment or **polarization**, characterizing a particular object in a certain environment [2].

Flux sources, which are simpler conceptually, usually have little physical meaning and resemble mathematical devices for setting up a real flow situation. Circulation sources are physically evident as vortex lines which have a clearer manifestation and actually exist in a real flow with rotation. The contribution of this paper is to show how weak vorticity in an inviscid flow interacts with a solid object. The results are of a general nature and apply to objects of any shape. Vorticity is bound in the fluid and is "entrained" by the object in much the same way as fluid is entrained by "drift". The added mass tensor provides the theoretical key to the solution of both problems.

FLUX SOURCES

An object of volume V moving at velocity $\mathbf{v}$ in an irrotational flow may be generated by internal sources and sinks of strength m_i located at $\mathbf{r}$.

The dipole moment of these sources is [1]

$$\mathbf{D} = \int \mathbf{r} m_i = \int \phi \mathbf{ds} + V\mathbf{v} \tag{1}$$

If the object is moving in an extensive fluid at rest far away, the added mass tensor $\underline{\underline{C}}$ is defined by

$$\int \phi \mathbf{ds} = \underline{\underline{C}} \cdot \mathbf{v}V \tag{2}$$

which does not depend on the details of conditions "at infinity" in the way that the induced net momentum does. Because of the linearity of Laplace's equation in this situation we may define the **polarizability**, $\underline{\underline{D}}$, such that

$$\mathbf{D} = \underline{\underline{D}} \cdot \mathbf{v}V \tag{3}$$

Combining (1) to (3) the two tensors are simply related by

$$\underline{\underline{D}} = \underline{\underline{C}} + \underline{\underline{I}} \tag{4}$$

Since $\underline{\underline{C}}$ is a symmetric tensor depending only on the shape of the object, so is $\underline{\underline{D}}$.

When the same object is at rest in fluid with a uniform velocity $\mathbf{U}$ far away, the sources and sinks are the same and dependent on the relative motion so that

$$\mathbf{D} = -\underline{\underline{D}} \cdot \mathbf{U}V \tag{5}$$

The force on a flux source is $-\rho \mathbf{U} m_i$. Forces between sources are mutual and cancel. There is no net force from the fluid on the sources (i.e., on the object) because $\sum m_i = 0$. The moment of the forces from the fluid on the object is, using (4) and (5),

$$\begin{aligned} \mathbf{M} &= -\sum \mathbf{r} \times \rho \mathbf{U} m_i = \rho \mathbf{U} \times \sum \mathbf{r} m_i \\ &= \rho \mathbf{U} \times \mathbf{D} = -\rho V \mathbf{U} \times \underline{\underline{D}} \cdot \mathbf{U} = \rho V \mathbf{U} \cdot \underline{\underline{C}} \times \mathbf{U} \end{aligned} \tag{6}$$

which is a compact version of the result given by Lamb [3].

When the object is in an irrotational flow that varies slowly on the scale of the object and can be described by a velocity

$$\mathbf{u} = \mathbf{U} + \mathbf{r} \cdot \nabla \mathbf{U} \tag{7}$$

before insertion of the sources, the resultant force is

$$F_p = \sum -\rho(m_i + m_i')(\mathbf{U} + \mathbf{r} \cdot \nabla \mathbf{U}) \tag{8}$$

where m_i' represents a small perturbation,with $\sum m_i' = 0$, in response to the gradient in the external field. To first order, (8) reduces to

$$\mathbf{F}_p = -\rho \sum m_i \mathbf{r} \cdot \nabla \mathbf{U} = -\rho \mathbf{D} \cdot \nabla \mathbf{U} \tag{9}$$

which we call the "polarization force" representing an interaction between the polarization and the external velocity gradient. Using (4) and (5), (9) can be put in the form

$$\mathbf{F}_p = \rho V(\mathbf{U} \cdot \nabla \mathbf{U} + \mathbf{U} \cdot \underline{\underline{C}} \cdot \nabla \mathbf{U}) \tag{10}$$

where the first term is the "buoyancy" force due to the external pressure gradient and the second term is compatible with a result derived by Taylor [4] and described by Lamb [3] in the alternative form

$$\mathbf{U} \cdot \underline{\underline{C}} \cdot \nabla \mathbf{U} = \nabla(\frac{1}{2}\mathbf{U} \cdot \underline{\underline{C}} \cdot \mathbf{U}) \tag{11}$$

which follows because $\underline{\underline{C}}$ is symmetric and $\nabla \times \mathbf{U} = 0$ in an irrotational flow.

CIRCULATION SOURCES

When a flow is rotational it contains vortices (circulation sources) that travel with the fluid. If a certain vortex line is marked, it will follow a trajectory which is the same as for a "time-line" recording the position of elements of fluid composing the vortex at subsequent intervals of time. If the vorticity is weak, these trajectories are determined by the "main" flow, the effect of vortices on each other being small. This picture formed the basis of Lighthill's analysis [5] of the wake of an object in a shear flow, and was later used by Auton [6] to derive the "lift" force on a sphere.

A vortex line passing close to an object will be deformed and will "drift" just as elements of fluid do. The velocity field from the vortex may be countered by internal sources m_i'. Since these have zero total sum and are "small" for "small" vorticity they contribute no net force, as in (8), to first order. Moreover, in an inviscid fluid, no net circulation is generated on the object. "Bound" vorticity would have to be generated some other way and it not part of the present analysis.

CROSS-STREAM VORTICITY

Let the main flow past a stationary object have velocity $\mathbf{U}$ in the x-direction. Let the oncoming flow have uniform vorticity in the cross-stream z-direction. Because of the component C_{xx} of the added mass coefficient, and the resulting impulse on the fluid by way of (2), there is a drift volume in the wake of the object representing fluid, and corresponding vorticity, that is retarded by the presence of the object.

We now consider a rectangular control volume around the object, with faces normal to the coordinate axes and large compared with the object. The total z-direction vorticity in this volume is augmented by an amount $C_{xx}V\omega_z$ because of the drift of fluid into this volume, as described by Lighthill [5] and sketched in Figure 1. The corresponding perturbations in velocity on the boundaries of the control volume may be determined from the basic equation of vector field theory:

$$\int \boldsymbol{\omega} dV = -\int \mathbf{u} \times \mathbf{ds} \tag{12}$$

This is to be applied to the z-component of vorticity, and therefore picks up the following components on the x- and y-faces of the control volume,

$$C_{xx}V\omega_z = \int \omega_z dV = \int \tilde{u}_y ds_x - \int \tilde{u}_x ds_y \tag{13}$$

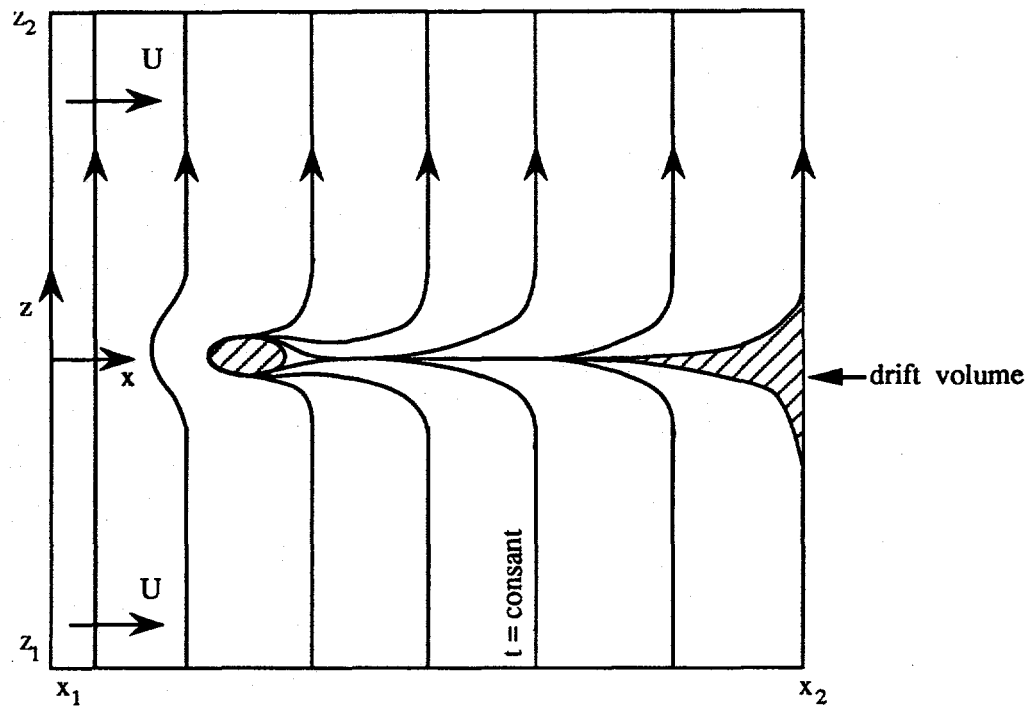

Figure 1. Vortex Lines, Originally in the z-Direction, Stretched Around an Object and Entrained by Drift in the Wake

Multiplying by ρU we get

$$\rho V C_{xx} U \omega_z = \int \rho U \tilde{u}_y ds_x - \int \rho U \tilde{u}_x ds_y \tag{14}$$

Now, on the y-faces far from the object the main flow is in the x-direction and therefore the perturbation in pressure is given by Bernoulli's equation as

$$\tilde{p} = -\rho U \tilde{u}_x \tag{15}$$

Using (15) in (14), the right-hand side is recognizable as the sum of the y-direction momentum flux through the x-faces and the pressure over the y-faces, which are exactly the terms in a momentum balance which shows the "drift" force from the fluid on the object in the y-direction to be,

$$F_{dy} = -\rho V C_{xx} U \omega_z \tag{16}$$

A more detailed derivation of this force is given in [7], where it is also related to the x-component of vorticity induced in the wake by bending of the vortex lines, originally in the z-direction. This x-vorticity in the wake loops around the object, the overall appearance resembling the bound vorticity and trailing vortex system for a conventional lifting surface.

Now, if the object is not oriented with one of its principal axes of added mass in the direction of the main flow, there will also be components of "interphase impulse", given by (2), in the transverse directions. For instance, the component C_{xy} (since $\underline{\underline{C}}$ is symmetric, it is not necessary to be fussy about the order of the subscripts) leads to displacement of the fluid streamlines in the y-direction due to relative velocity in the x-direction. The z-direction vortex lines that were

parallel upstream of the object are then bent in the wake as a result of this transverse "drift". If we look upstream in the negative x-direction from the far wake, these vortex lines will all be bent into the same shapes, independent of x, and form a set of vortex sheets, representing "streamlines" for vorticity (Figure 2). The z-direction vorticity in the wake is related to the corresponding velocity variations by

$$\omega_z = \frac{\partial u_y}{\partial x} - \frac{\partial u_x}{\partial y} \tag{17}$$

but $\partial u_y/\partial x = 0$ in a fully-developed wake and therefore

$$u_x = -\int \omega_z dy \tag{18}$$

The right hand side of (18) represents the z-vorticity flux which is constant along a "streamline" for vorticity. Therefore the cross-sections of vortex sheets in Figure 2 also represent contours of constant u_x. The perturbation in u_x is

$$\tilde{u}_x = -\int \tilde{\omega}_z dy = \omega_z Y \tag{19}$$

where Y is the displacement of a vortex line now lying at the point of interest. When (19) is integrated over the entire face of the control volume lying in the wake, there is a perturbation in outgoing mass flux in the amount

$$\dot{m} = \rho \int \tilde{u}_x dy dz = \rho\omega_z \int Y dy dz = -\rho\omega_z V C_{xy} \tag{20}$$

where the concept of "drift volume" in the y-direction has been used. The negative sign is needed because $\mathbf{v}$ in (2) is replaced by $-\mathbf{U}$. The increased mass flux $\dot{m}$ comes from fluid that is drawn into the sides of the control volume. The mechanism for "pumping" this secondary flow is the perturbation in vorticity in the wake. These perturbations form loops in the y-z plane that add to the original uniform vorticity to produce the pattern shown in Figure 2. In the extended wake these loops form cylindrical sheets of secondary vorticity that generate axial velocity much as the coils on a solenoid generate its axial magnetic field.

A fully developed wake cannot maintain pressure perturbations (which would lead to further "development") and the momentum flux out of the control volume on the wake side is increased by

$$\rho \int \left[(U + \tilde{u})^2 - U^2\right] dy dz = 2U\dot{m} \tag{21}$$

Combining (21) with the flux of momentum into the sides of the control volume, $\rho U\dot{m}$, the net force due to velocity perturbations induced by vorticity is

$$F_{dx} = \rho V U C_{xy} \omega_z \tag{22}$$

Results similar to (16) and (22) follow if there is vorticity in the transverse y-direction.

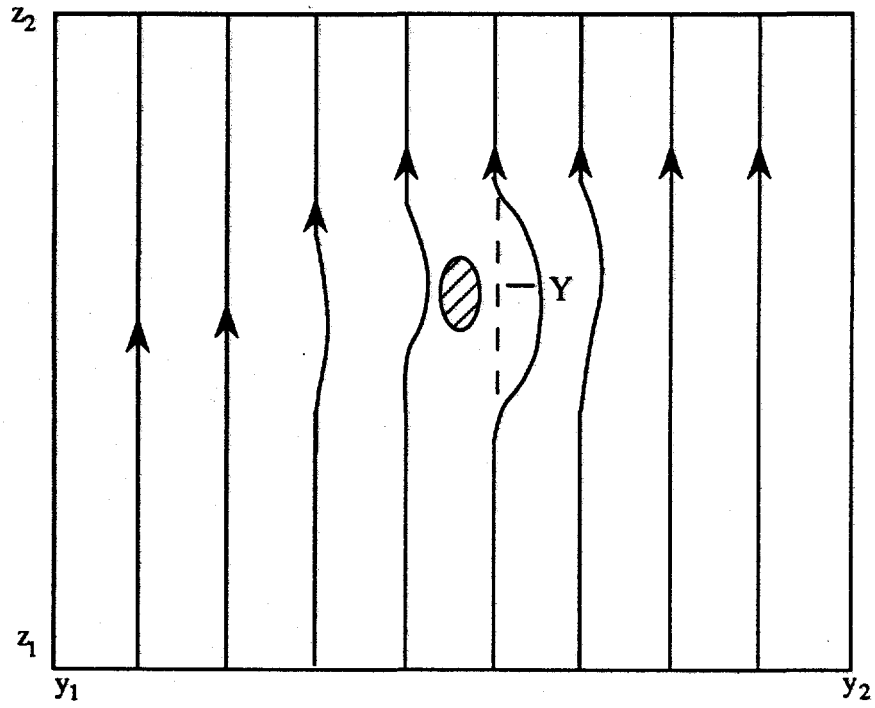

Figure 2. Drift of z-Direction Vortex Lines in the y-Direction Behind an Asymmetric Object

STREAMWISE VORTICITY

A uniform upstream vorticity ω_x is carried along the streamlines of the primary flow and will be diverted sideways in the wake if there are components C_{xy} and C_{xz} to the added mass tensor. The effect of C_{xy} is to displace streamlines in the y-direction, which can also be represented by Figure 2 which now represents the location in the wake of vortex sheets originally in the x-z plane. These contours now represent constant values of $\tilde{u}_z$ in the amount $-Y\omega_z$, by arguments resembling those leading to (19). This produces negligible effect on the sides of the control volume but introduces a perturbation in the flux of z-momentum in the wake and a corresponding drift force in the amount

$$F_{dz} = \rho V U C_{xy} \omega_x \tag{23}$$

similar effects occur if there is a C_{xz}, with corresponding results.

SYNTHESIS

All of the components of "drift force" derived above may be added together, assuming each is small so that interactions can be neglected, to give

$$\mathbf{F}_d = \rho V \mathbf{U} \cdot \underline{\underline{C}} \times \omega \tag{24}$$

This must be added to the polarization force in (10) to obtain the net force

$$\mathbf{F} = \rho V (\mathbf{U} \cdot \nabla \mathbf{U} + \mathbf{U} \cdot \underline{\underline{C}} \cdot \nabla \mathbf{U}^T) \tag{25}$$

Since $\underline{\underline{C}}$ is symmetric, the second term in (25) is exactly equal to Taylor's Force derived in (11) for inviscid flows. Therefore Taylor's Force is equally valid in flows with weak rotation.

DISCUSSION

The derivations in this paper are given with more detail in [7] where they are shown to be compatible with Auton [6] and Auton et al. [8]. Some results are derived there for an oncoming shear flow passing over an object in a tube, showing that it is not necessary for the control volume to be "large" or for the flow to be unbounded.

The quantity appearing in $\frac{1}{2}\mathbf{U}\cdot\underline{\underline{C}}\cdot\mathbf{U}$, when multiplied by ρV, has the form of the "kinetic energy due to relative motion" which plays a key role in effective continuum conservation equations for inviscid two-phase dispersions developed by Geurst [9,10] and Wallis [11,12]. Indeed, the forces described by (24) and (25) are recovered from Wallis [12], equation (87), in the limit when $\underline{\underline{C}}$ is isotropic, the volume of the particle is constant, there is no unsteady flow and the particle is at rest. Geurst's equations have the desirable property of being objective. It appears that the drift force is necessary in order to make the overall interaction force objective, as discussed in a more restricted case by Drew and Lahey [13,14].

Since the mean pressure gradient in the fluid flow is

$$\nabla\overline{p} = -\rho\mathbf{U}\cdot\nabla\mathbf{U} \tag{26}$$

the force in (25) is equivalent to minus the volume of the object times the gradient of a "particle pressure":

$$p_p = \overline{p} - \frac{1}{2}\rho\mathbf{U}\cdot\underline{\underline{C}}\cdot\mathbf{U} \tag{27}$$

which can be shown (Wallis [15]) to be the same as the mean bulk stress in the object when a uniform flow is oriented along a principal axis of $\underline{\underline{C}}$ and no external forces act on the object, or more generally when the restraining torque in (3) is applied by simple couples composed of equal and opposite forces acting perpendicular to a lever arm between them.

ACKNOWLEDGEMENT

This work was performed under the U.S. Department of Energy, Contract #DE-FG02-86ER13528, administered by Dr. Oscar Manley.

REFERENCES

1. Cai, X. and G.B.Wallis 1993 The Added Mass Coefficient for Rows and Arrays of Spheres Oscillating Along the Axes of Tubes, *Phys. Fluids A* **A5** (7), 1614-1629.

2. Wallis, G.B. 1993 The Concept of Polarization in Dispersed Two-Phase Potential Flow, *Nuclear Engineering and Design*, **141**, 329-342.

3. Lamb, H. 1932 *Hydrodynamics*, 6th ed., Cambridge University Press.

4. Taylor, G.I. 1928 The Forces on a Body Placed in a Curved or Converging Stream of Fluid. *Proc. Roy. Soc.*, **A120**, 260-283.

5. Lighthill, J. 1956 Drift, *J. Fluid Mechanics*, **1**, 31-53.

6. Auton, T.R. 1987 The Lift Force on a Spherical Body in a Rotational Flow, *J. Fluid Mech.*, **183**, 199-218.

7. Wallis, G.B. 1995 The Drift Force on an Object in an Inviscid Weakly-Varying Incompressible Flow, being revised for *J. Fluid Mechanics.*

8. Auton, T.R., Hunt J.C.R. and Prud'homme, M. 1988 The Force Exerted on a Body in Inviscid Unsteady Non-uniform Flow, *J. Fluid Mechanics*, **197**, 241-257.

9. Geurst, J.A. 1985 Virtual Mass in Two-Phase Bubbly Flow, *Physica*, **129A**, 233-261.

10. Geurst, J.A. 1986 Variational Principles and Two-Fluid Hydrodynamics of Bubbly Liquid/Gas Mixtures, *Physica*, **135A**, 455-486.

11. Wallis, G.B. 1989 Inertial Coupling in Two-Phase Flow: Macroscopic Properties of Suspensions in an Inviscid Fluid, *Multiphase Science and Technology*, **5**, 239-361.

12. Wallis, G.B. 1991 The Averaged Bernoulli Equation and Macroscopic Equations of Motion for the Potential Flow of a Dispersion, *Int. J. Multiphase Flow*, **17**(6), 683-695.

13. Drew, D.A. and Lahey, R.T., Jr. 1987 The Virtual Mass and Lift Force on a Sphere in Rotating and Straining Inviscid Flow, *Int. J. Multiphase Flow*, **13**, 113-121.

14. Drew, D.A. and Lahey, R.T., Jr. 1990 Some Supplemental Analysis Concerning the Virtual Mass and Lift Force on a Sphere in a Rotating and Straining Flow, *Int. J. Multiphase Flow*, **16**, 1127-1130.

15. Wallis, G.B. 1994 The Particle Pressure of Arrays in a Potential Flow, *Nuclear Engineering and Design*, **151**, 1-14.

ACTIVE CONTROL of CONVECTION

Haim H. Bau

Department of Mechanical Engineering and Applied Mechanics, University of Pennsylvania, Philadelphia, PA 19104-6315

ABSTRACT

Using stability theory, numerical simulations, and in some instances experiments, it is demonstrated that the critical Rayleigh number for the bifurcation (i) from the no-motion (conduction) state to the motion state and (ii) from time-independent convection to time-dependent, oscillatory convection in the thermal convection loop and Rayleigh-Bénard problems can be significantly increased or decreased. This is accomplished through the use of a feedback controller effectuating small perturbations in the boundary data. The controller consists of sensors which detect deviations in the fluid's temperature from the motionless, conductive values and then direct actuators to respond to these deviations in such a way as to suppress the naturally occurring flow instabilities. Actuators which modify the boundary's temperature/heat flux are considered. The feedback controller can also be used to control flow patterns and generate complex dynamic behavior at relatively low Rayleigh numbers.

INTRODUCTION

Until recently, most of the scientific community's work in the convection field has focused on identifying and describing various physical phenomena. In contrast, our work focuses on directing convective systems to behave in desired ways. The ability to control flow patterns is important from both the technological and the theoretical points of view. In many material processing applications, convection plays an important role. The ability to control the flow may lead to better quality products and more economical processes than are currently possible. In some processes, it may be desirable to operate at Rayleigh (R) numbers higher than the one at which convection occurs and yet have no convection. In other processes, it may be desirable to suppress (laminarize) chaotic or turbulent motions and maintain a steady, time-independent flow in order to minimize flow unpredictability, remove temperature oscillations which may exceed safe operational conditions, and/or reduce drag. In still other processes, it may be advantageous to induce chaos, under conditions at which it would not normally occur, so as to enhance mixing, heat transport or chemical reactions. From the theoretical point of view, the ability to control the transition and routes to chaos and to stabilize otherwise nonstable equilibrium states may assist us in obtaining a better understanding of the dynamics of convective systems and the transition to turbulence.

Our work on active feedback control of convection has focused on two simple paradigms: the thermal convection loop which is an experimental analog of the celebrated Lorenz equations [1] and

the classical Rayleigh-Bénard problem. The thermal convection loop has the advantage that its flow dynamics can be approximated by a low-dimension, dynamic model and that the theoretical predictions can be verified by relatively simple experiments. After succeeding in controlling flow patterns in the thermal convection loop, we utilized the physical insights we gained there to modify the flow patterns of a more complicated convective system, the Rayleigh-Bénard problem which is a paradigm of convective phenomena occurring in various material processes. Our work on these problems had proven applicable to other flow phenomena as well. For instance, we have successfully demonstrated that the loss of stability of planar Poiseuille flow can be significantly delayed or advanced through active feedback control [2].

THE THERMAL CONVECTION LOOP

The thermal convection loop is made of a pipe, bent into a torus, standing in the vertical plane. The lower and upper halves of the torus are heated and cooled, respectively. The heating and cooling conditions are symmetric with respect to the loop axis that is parallel to the gravity vector. In the absence of a controller, as the temperature difference between the heated and cooled sections of the thermal convection loop increases, the flow in the loop changes from no-motion to steady, time-independent motion to temporally oscillatory, chaotic motion with occasional reversals in the direction of the flow. The bifurcation diagram of the uncontrolled system is depicted in Fig. 1. With the use of a feedback controller making small perturbations in the boundary conditions, we have demonstrated that it is possible to:

(i) maintain the no-motion state at significantly higher temperature differences between the heated and the cooled portions of the loop than the critical one corresponding to the onset of convection in the uncontrolled system [3];
(ii) maintain steady, time-independent flow under conditions in which the flow would otherwise be chaotic [4,5].
(iii) stabilize periodic, non-stable orbits which exist in the chaotic regime of the uncontrolled system [3];
(iv) induce chaos in otherwise laminar (fully predictable), non-chaotic flow [5]; and
(v) render a subcritical bifurcation supercritical through the use of a nonlinear controller [6].

To make some of this work more concrete, we report in Figs. 2-4 a sample of our observations. Fig. 1 depicts the bifurcation diagram for the flow in the uncontrolled loop. For Rayleigh numbers $R<R_1$, the no-motion state is globally stable. As R is increased above R_1, the no-motion state loses stability and is replaced by time-independent motion either in the clockwise or the counterclockwise direction. When R is further increased to $R=R_2$, a second bifurcation occurs, and the time-independent motion loses stability. The loss of stability occurs through a subcritical Hopf bifurcation into a non-stable, limit cycle. Above R_2, the time-independent motion is replaced with a complicated time-dependent, chaotic motion. Fig. 2 depicts the experimentally observed temperature difference ($\Delta T_{3\text{-}9}$) between positions *3* and *9* o'clock around the loop as a function of time in the chaotic regime of the uncontrolled system. Changes in the sign of $\Delta T_{3\text{-}9}$ indicate a change in the flow direction. When $\Delta T_{3\text{-}9}>0$ (<0), the flow is in the counterclockwise (clockwise) direction. Fig. 3 shows the effect of the controller. To highlight this effect, the figure depicts the experimentally measured $\Delta T_{3\text{-}9}$ as a function of time both before and after the activation of the controller. Witness that once the controller has been engaged, the seemingly random, violent oscillations of Fig. 2 disappear and the flow is laminarized. The boundary conditions corresponding to Fig. 2 were altered only slightly to produce the almost time-independent flow shown in Fig. 3 for $t>33$ minutes. The feedback controller operates by sensing any deviation of $\Delta T_{3\text{-}9}$ from its desired value and altering slightly the heating rate, according to a prescribed control rule, in such a way as to nullify the deviation. The observed behavior is in agreement with our theoretical predictions.

The Hopf bifurcation occurring in the thermal convection loop as well as in many other flow systems (i.e., shear flows) is subcritical. In the case of subcritical bifurcations, often the size of the domain of attraction of the time-independent state is limited. In fact, in shear flows, the transition to turbulence typically occurs at subcritical Reynolds numbers. This is apparently due to disturbances

which grow sufficiently large so as to escape the domain of attraction of the laminar state and cause the system to snap through the nonstable limit cycle to a possibly chaotic or turbulent attractor. In order to increase the domain of attraction of the time-independent state, we drew inspiration from [7] and used nonlinear control to render the subcritical bifurcation supercritical. The bifurcation diagram of the thermal convection loop with and without nonlinear (cubic) control is depicted in Fig. 4. The theoretical predictions were successfully verified in experiments.

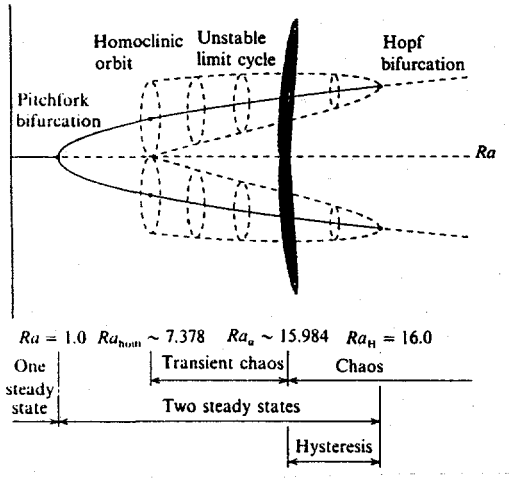

Fig. 1: The (unscaled) bifurcation diagram depicting various flow patterns in the uncontrolled loop as a function of the Rayleigh number. Stable and nonstable states are denoted by solid and dashed lines, respectively. The dark region represents the appearance of the strange attractor, which exists for $R>Ra_a$.

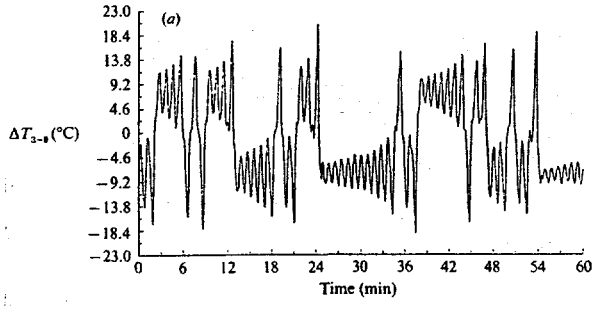

Fig. 2: The experimentally observed temperature difference, $\Delta T_{3\text{-}9}$, is depicted as a function of time for the uncontrolled thermal convection loop.

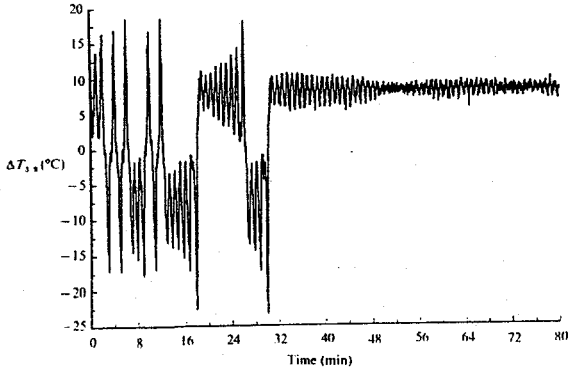

Fig. 3: The experimentally observed temperature difference, $\Delta T_{3\text{-}9}$, is depicted as a function of time both before and after activation of the controller. The controller was activated 33 minutes into the run. Observe the difference between the chaotic oscillations and the controlled (laminarized) flow.

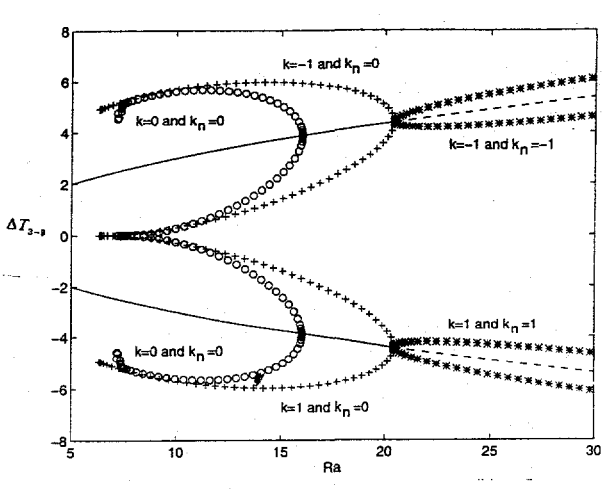

Fig. 4: The Hopf bifurcation in the thermal convection loop problem is shown without control $\{k, k_n\}=\{0,0\}$, with linear proportional control $\{k, k_n\}=\{-1,0\}$, and with linear and nonlinear controllers $\{k, k_n\}=\{-1,-1\}$. k and k_n denote, respectively, the linear and nonlinear controller gains.

THE STABILIZATION OF THE NO-MOTION STATE IN THE RAYLEIGH-BÉNARD PROBLEM

Encouraged by our success with the thermal convection loop, we implemented similar ideas in two more complicated flow systems: the Rayleigh-Bénard problem of a Newtonian fluid and the Lapwood problem of a saturated porous medium heated from below and cooled from above. In both cases, as the Rayleigh number, R, increases, the uncontrolled system undergoes a sequence of bifurcations from no-motion to time-independent motion (at $R=R_1$) to time-dependent motion (at $R=R_2$). The magnitude of R_1 depends on the container's geometry. The magnitude of R_2 depends on both the container's geometry and the fluid's Prandtl number (Pr). As the Prandtl number decreases so does the magnitude of R_2. In this section, we describe the stabilization of the no motion state. In other words, we use a controller to increase the magnitude of R_1.

The controller consists of sensors and actuators. The bottom surface consists of individual heaters, each equipped with a separately controlled power supply. The heaters serve a dual purpose. They supply the nominal heat flow needed to drive the convection as well as serve as actuators which effectuate the control. The sensors are diodes embedded on the heated surface and located at the layer's mid-height. They detect deviations in the fluid's temperature from the desired conductive values and direct the actuators to act in such a way as to enhance the disturbance-dissipating mechanisms in the fluid. More specifically, when the sensors detect an increase (decrease) in the fluid's temperature caused by an ascending (descending) column of fluid, they direct the actuators to reduce (increase) slightly the container's bottom temperature beneath the ascending (descending) fluid column. Through this action, the buoyant forces are reduced, thereby increasing the time available for conduction to dissipate disturbances before they have the opportunity to manifest themselves. Once the disturbances have been dissipated, the container's bottom temperature is restored to its nominal, uniform value.

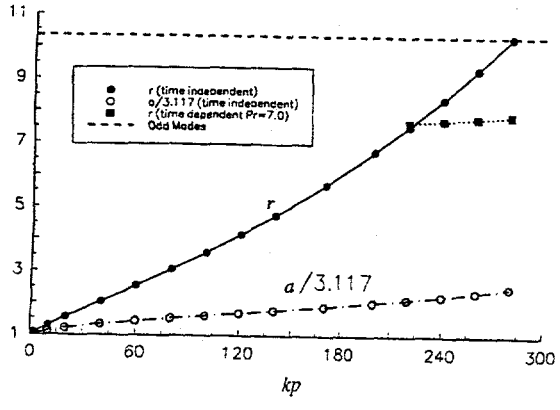

Fig. 5: The normalized critical Rayleigh ($r=\frac{R}{1707.762}$) and wave ($a/3.117$) numbers are depicted as functions of the thermal controller's gain (Kp) for $Pr=7$. The solid and dotted curves describe the loss of stability through, respectively, a simple eigenvalue (exchange of stability) and a Hopf bifurcation. The dashed curve describes loss of stability of the first odd mode.

For example, in the case of a linear, proportional control, the control law can be written as $\tilde{q}=\mathbf{K}\tilde{e}$ where $\tilde{e}$ is a n-dimensional vector describing the deviations of the measured temperatures from their desired values, $\tilde{q}$ is a m-dimensional vector describing the actuators' output, and $\mathbf{K}$ is a $m\times n$ matrix whose entries are the controller gains. The simplest situation, which we have studied thus far, is that of a single sensor being linked to a single actuator through a feedback loop. In such a case, the matrix $\mathbf{K}$ is square and diagonal. In the future, we will also study other scenarios such as when the matrix $\mathbf{K}$ is not diagonal as well as nonlinear control schemes.

Due to its accessibility to analytical treatment, we initially focused our attention on the problem of an unbounded, horizontal fluid layer. Using linear stability analysis, we first demonstrated that R_1, in a saturated porous layer (the Lapwood problem) could be significantly increased [8]. The porous media problem was studied for three reasons: (i) it is relevant to various technological processes such as transport in the mushy region of solidification processes and gel electrophoresis of macromolecules; (ii) it allows simpler and more complete analytic treatment; and (iii) if necessary, experiments in porous media can be conducted in a cruder and less expensive apparatus than would be required in the Newtonian fluid case since the onset of convection in porous media occurs at much higher temperature differences between the container's bottom and top than it does in a Newtonian fluid.

Subsequently, we carried out stability analyses of the controlled, no-motion state of a Newtonian fluid (the Rayleigh-Bénard problem) heated with a uniform temperature [9,10] and with uniform flux [11]. For example, for the uniform temperature heating and cooling, we demonstrated that the critical Rayleigh number for the onset of convection can be postponed from *1708* (in the uncontrolled system) to at least about *17,000* (in the controlled system). It is likely that with more sophisticated control strategies than the ones we have used, additional increases in R_1 would be possible. Fig. 5 depicts a stability diagram which shows the normalized Rayleigh number ($R_1/1708$) as a function of a proportional controller gain.

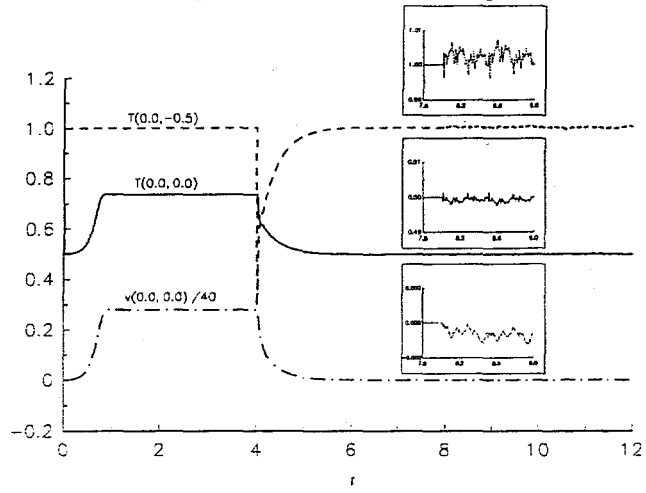

Fig. 6: The temperatures, $T(0,0)$ (solid line) and $T(0,-0.5)$ (dashed line), and the , vertical velocity $v(0,0)$ are depicted as functions of nondimensional time (t) for $R=3000$ and $Pr=0.7$. For $0<t<4$, the controller is off. For $4<t<8$, the controller with gain A is active. For $t>8$, the controller counteracts the action of random disturbances.

In order to study the supercritical flow dynamics in the uncontrolled and controlled systems and the stability in cylindrical containers, we developed numerical codes. The numerical simulations demonstrated that the controller can successfully suppress non-linear disturbances. Fig. 6 illustrates the controlled system's response to random disturbances. For Rayleigh number, $R=3000$, $Pr=0.7$, and controller gain $Kp=3$, Fig. 6 depicts, as functions of time (t), the mid-height temperature (solid line), the bottom temperature (dashed line), and the mid-height, vertical velocity (dot-dashed line) on the left hand side of the computational domain. For the controlled system, the critical Rayleigh number, wavenumber, and cell width are, respectively, $Rc=3538$, $a_c=3.877$, and $L_x=0.81$.

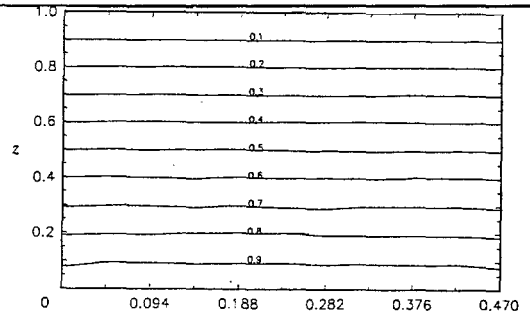

Fig. 7: The temperature field (isotherms) for $R=10,000$ and $Pr=0.7$ in the presence of a controller with gain $K_p=8.0$ and random fluctuations in the temperature field. The almost horizontal isotherms indicate lack of convection. This figure should be contrasted with Fig. 8.

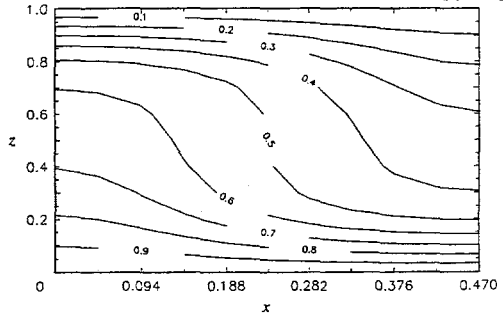

Fig. 8: The temperature field (isotherms) associated with time-independent flow in the absence of a controller for $R=10,000$ and $Pr=0.7$. The boundary conditions are similar to the ones in Fig. 7.

The initial conditions in Fig. 6 correspond to a no-motion state (t=0). In the beginning, the controller is off and the nondimensional bottom ($z=-0.5$) temperature is uniform, $T(0,-0.5)=1$. As a result of a thermal disturbance intentionally introduced at point $(0,0)$, counter-clockwise motion begins. In order to contrast the controlled and uncontrolled states, we allow the motion state to achieve equilibrium (this normally will never happen when the controller is active). At time $t=4$, the proportional controller with a gain $Kp=3$ is switched on. Since, in this case, we are dealing with established motion, the controller alters significantly the container's bottom temperature. This alteration in the container's bottom temperature causes a prompt reduction in the buoyancy force,

which, in turn, causes the flow to slow down. This slow down provides sufficient time for thermal dissipation to restore the conductive temperature field. As a result, the motion is successfully suppressed. The fact that the controller succeeded in suppressing an established motion suggests that it has a large domain of attraction. Once the motion has been suppressed, the controller restores the bottom's nondimensional temperature to its nominal, uniform value of *1*, the mid-plane's nondimensional temperature to its conductive value of *0.5*, and the vertical velocity to its no-motion value of zero. A glance at the temperature field (not shown here) reveals perfectly horizontal isotherms. In other words, for $4<t<8$, a stable, no-motion state is sustained for supercritical Rayleigh numbers with boundary conditions identical to the ones of the uncontrolled system.

We also tested the controller's response to small disturbances for $t>8$. We introduced random fluctuations in the temperature of magnitude up to $\pm 1\%$. Despite these disturbances, the container's bottom temperature remained close to its nominal value of one and there was essentially no motion in the fluid. In order to illustrate the temperature and velocity variations, it was necessary to stretch the vertical axis (see the insert in Fig. 6).

Fig. 7 depicts a snapshot of the temperature field (isotherms) for a controlled layer ($Kp=8$) with $R=10{,}000$ ($r\sim 5.85$). The temperature field was subject to random disturbances of magnitude up to $\pm 1\%$ of the grid point's temperature. The fact that the isotherms remained essentially horizontal suggests the absence of convective motion. This figure should be contrasted with Fig. 8 which depicts the temperature field for the same conditions in the absence of a controller. Fig. 7 clearly illustrates that the controller has successfully maintained a no-motion state under conditions in which convection normally would occur.

Although the controller preserves the classical no-motion state of the Rayleigh-Bénard problem, it has a profound effect on the supercritical behavior. The stability diagrams indicate that the controller can cause a transition from the no-motion state to complicated, time-dependent, supercritical motions at relatively low Rayleigh numbers. This suggests yet another potential application of the controller. Rather than stabilizing an equilibrium state of a given system, the controller could be used to create flow structures to suit particular requirements.

Before constructing an experimental apparatus to verify the numerical predictions, we needed to determine the optimal number and location of the sensors and actuators required to effectuate the control. We modified our numerical codes to analyze 3-D convection in an upright, circular cylinder. Preliminary results were presented in [12]. Since the three-dimensional, time-dependent computations required a considerable amount of computer time, a great effort went into code optimization. Computations have been carried out to determine the magnitudes of R_1 and R_2 as functions of apparatus geometry, various control strategies, the number of sensors and actuators, and potential time delays.

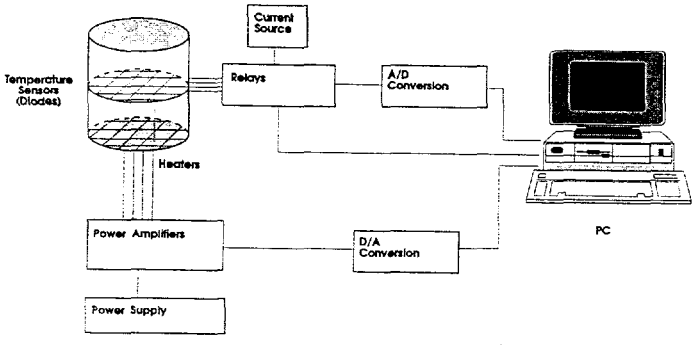

Fig. 9: A schematic description (not drawn to scale) of the experimental set-up.

We are now in the process of constructing an experimental apparatus. The experimental set-up is described schematically in Fig. 9. Briefly, the experimental apparatus consists of an upright cylinder, *0.06m* in diameter, heated from below and cooled from above. The height of the fluid layer and the aspect ratio of the apparatus (radius/height) can be varied. About *40* sensors and *40* actuators are used to facilitate the control. The bottom of the apparatus contains a network of individually controlled heaters.

The need to use a relatively large number of sensors and actuators has required us to devise novel solutions. Since we were not able to purchase the necessary actuators, we were forced to microfabricate them ourselves. The heaters were manufactured by growing an oxide layer on the back of a silicon wafer and spattering a thin nichrome layer on top of the oxide. Using photolithography, we shaped the heaters to the desired form. Next, we spattered silicon nitride on top

of the nichrome layer and etched windows in the silicon nitride to allow the deposition of gold electrodes on top of the heaters. The electrodes are used to assure uniform current density in each heater. Bonding pads were deposed on top of the silicon nitride layer to accommodate electrical leads for the supply of power .

Our theoretical studies suggest that the most effective location of the sensors is at the fluid layer's midheight. We have selected diodes to serve as temperature sensors. Because the diodes allow only unidirectional current flow, we have been able to significantly reduce the number of lead wires and multiplexer channels compared to what would be required if we were to use other sensing devices such as thermistors and/or thermocouples. The diodes are interconnected with two sets of intersecting wires (Fig. 9). We denoted one set of parallel wires with letters *A, B,* ... and the other set with numbers *1, 2,....* The temperature sensed by diode *C4* can be read by measuring the potential across wires *C* and *4*. In order to measure n^2 diodes, we need only two sets of n intersecting wires and a multiplexer with $2n$ channels. In contrast, if we were to use thermistors or thermocouples, the number of lead wires and multiplexer channels would be proportional to n^2. We tested the operation of the diode arrays, individually calibrated the diodes, and demonstrated that we can detect temperatures with a precision better than *0.01K*.

Via a multiplexer, the sensors' output is transmitted to a computer. Any of the sensors can control any of the actuators. According to a predetermined control law, the computer modulates the actuators' power.

For the onset of convection experiments, we will use Dow-Corning 200 fluids. We can customize the fluid to obtain the desired temperature difference between bottom and top at the onset of convection. For example, for Dow Corning 200 with a viscosity of *1000cs* and a layer height of *0.02m*, the critical temperature difference at onset is about *3K*.

Initially, experiments will be conducted in the absence of a controller to determine, as a function of the apparatus' aspect ratio and the working fluid, the critical Rayleigh numbers for the onset of convection in the uncontrolled system. A description of the post-critical flow patterns in our apparatus will also be obtained. The measured results will be compared with our theoretical predictions for the uncontrolled system. Subsequently, we will repeat the experiments in the presence of a controller and observe the effect of the controller on the stability of the no-motion state as well as on the supercritical flow patterns.

SUPPRESSION OF OSCILLATORY RAYLEIGH BÉNARD FLOWS

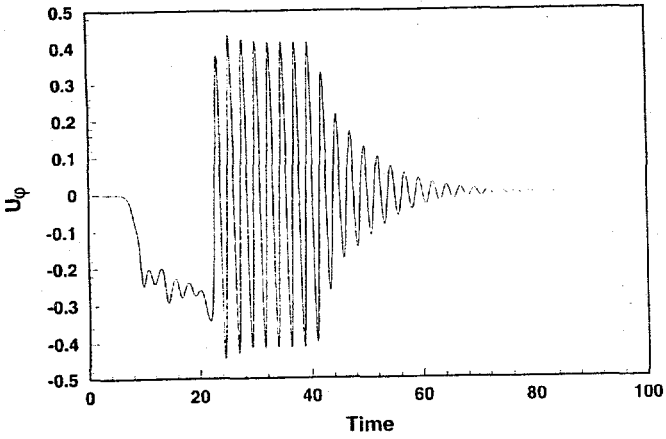

Fig. 10: The angular velocity u_ϕ at a point on the cylinder's midplane is depicted as a function of time. The system is (not) controlled for *(t<40) t>40. R=5000.*

Another objective of our research work is to delay or advance the secondary bifurcation from time-independent flow into oscillatory flow. The design of a controller is complicated by the fact that the system is highly nonlinear and closed form expressions for the time-independent flow from which the oscillatory flow bifurcates are not available. We are using the numerical code we described earlier to identify the critical Rayleigh numbers and the flow dynamics in an uncontrolled system. To verify the code we are comparing our theoretical predictions with experiments [13]. The numerical simulations allow us to obtain a wealth of information which can not be readily measured in experiments and enhance our understanding of the flow dynamics at high Rayleigh numbers.

For example, for a cylindrical container, with an aspect ratio (radius/height) of one, containing Newtonian fluid of *Pr=0.02* (i.e., gallium), we found that the first bifurcation from no-motion to time-independent motion occurs at $R_1 \sim 2200$. A second bifurcation from time-independent flow to

time-dependent flow occurs at $R_2 \sim 4800$. A sequence of additional bifurcations follows in quick succession until chaotic flow is observed for $R > 9000$.

For $R < R_2$, the flow consists of two counterrotating cells. With the onset of oscillatory behavior, the two cells oscillate angularly at relatively low amplitude. Using control strategies similar to ones we described in the previous section, we were able to suppress the oscillatory behavior. Fig. 10 depicts the angular velocity u_ϕ at a point on the cylinder's midplane for $R = 5000$. The initial conditions correspond to a no-motion state. For t<40, the system was not controlled and oscillatory motion has evolved. For $t > 40$, the controller is active. The controller successfully suppresses the oscillatory behavior and retains time-independent convection under the same conditions in which, in the absence of a controller the motion would have been oscillatory.

CONCLUSIONS

We have tackled the complicated problem of controlling highly nonlinear, distributed parameter systems. Through analysis, numerical simulations, and experiments (in the case of the thermal convection loop only), we have demonstrated that flow patterns can be controlled. Our immediate challenge now is to obtain experimental verification for our theoretical predictions for the Rayleigh Bénard problem. If successful, this research may provide the material processing community with an enabling technology.

ACKNOWLEDGMENT

Our work on the Rayleigh-Bénard problem was performed under the auspices of the U.S. Department of Energy.

REFERENCES

1. Lorenz, E. N., 1963, J. Atmospheric Sci. 20, 130-141.

2. Hu, H., and Bau, H. H., 1994, "Feedback Control to Delay or Advance Linear Loss of Stability in Planar Poiseuille Flow," Proceedings Royal Society A, 447, 299-312.

3. Singer, J. and Bau, H.H.,1991b, "Active Control of Convection," Physics of Fluids A, 3, 2859-2865.

4. Singer, J., Wang, Y-Z and Bau, H. H., 1991, "Controlling a Chaotic System," Physical Review Letters 66, 1123-1125.

5. Wang, Y-Z, Singer J., and Bau, H. H., 1992, "Controlling Chaos in a Thermal convection Loop," J. Fluid Mechanics, 237, 479-498.

6. Yuen, P., and Bau, H. H., 1995, "Rendering a Subcritical Bifurcation Supercritical," in preparation.

7. Abed, E. H., and Fu, J-H, 1986, "Local Feedback Stabilization and Bifurcation Control, I-Hopf Bifurcation," Systems Control Letters, 7, 11-17.

8. Tang, J., and Bau, H. H., 1993, "Feedback Control Stabilization of the No-motion State of a Fluid Confined in a Horizontal, Porous Layer Heated from Below," J. Fluid Mechanics, 257, 485-505.

9. Tang, J., and Bau, H. H., 1993, "Stabilization of the No-motion State in Rayleigh-Bénard Convection Through the use of Feedback Control," Physical Review Letters, 70, 1795-1798.

10. Tang, J., and Bau, H. H., 1994, "Stabilization of the No-motion State in the Rayleigh-Bénard Problem," Proceedings Royal Society A, 447, 587-607.

11 Tang, J., and Bau, H. H., 1995, "Stabilization of the No-motion state of a Horizontal Fluid Layer Heated from Below with Joule Heating," to appear in Trans. ASME-J. Heat Transfer.

12. Tang, J., and Bau, H. H., 1993, "Stabilization of the No-Motion State in Rayleigh-Bénard Convection in an Upright, Circular Cylinder," Fundamentals of Natural Convection, Boyd, R. D, and Kroeger, P. G., editors, ASME-HTD-264, 39-48.

13. Heslot, F., Casting, B., and Libchaber, A., 1987, "Transition to Turbulence in Helium Gas," Physical Review A, 36, 5870-5873.